nature communications

Article

https://doi.org/10.1038/s41467-026-70394-3

Solubility based mechanistic profiling of combinatorial drug therapy

Received: 14 August 2025

Accepted: 26 February 2026

Published online: 25 March 2026

Check for updates

Elham Gholizadeh[1,13], Ehsan Zangene[1,13], Uladzislau Vadadokhau[1], Danilo Ritz[2], Juho J. Miettinen[3], Rabah Soliymani[1], Marc Baumann[1], Mathias Wilhelm[4,5], Esko Kankuri[6], Paul A. Haynes[7], Caroline A. Heckman[3,8], Amir A. Saei[9,14] & Mohieddin Jafari[1,10,11,12,14]

Acute myeloid leukemia (AML) remains challenging to treat due to extensive genetic heterogeneity, high relapse rates, and treatment-related toxicity. Although drug combinations offer therapeutic promise, their selection is often empirical. Here, we introduce Combinatorial Proteome Integral Solubility/Stability Alteration analysis (CoPISA), a high-throughput proteomics workflow that captures protein solubility/stability alterations uniquely induced by drug combinations. We applied CoPISA to two rationally designed AML drug pairs, LY3009120-sapanisertib (LS) and ruxolitinib-ulixertinib (RU), previously identified as the most effective and least toxic combinations among many candidates and validated in AML cell lines, patient-derived samples and zebrafish xenograft models. We uncovered an emergent mechanism termed "conjunctional targeting", in which combinatorial drug action induces combination-exclusive protein targets consistent with an AND-gate logic model. LS-specific converged on SUMOylation, chromatin condensation, and VEGF-linked adhesion, while RU-specific targets disrupted DNA-damage checkpoints, mitochondrial bioenergetics, and RNA-splicing. Post-translational modification analysis revealed combination-induced acetylation, methylation, and phosphorylation of key AML proteins, including NPM1. Network analysis demonstrated that a substantial fraction of AML-associated proteins targeted by CoPISA are unique to combinations, including DNMT3A, NPM1, and TP53. By uncovering a mechanistic layer beyond classical synergy, CoPISA provides a robust framework for the precision-guided design of combinatorial therapies in heterogeneous cancers.

Acute myeloid leukemia (AML) is an aggressive hematologic malignancy characterized by the clonal expansion of immature myeloid cells in the bone marrow and peripheral blood, resulting in disrupted hematopoiesis[1]. Due to the complexity of AML and the limited efficacy of monotherapies, combination therapy has long been central to treatment strategies[2,3]. This approach often demonstrates superior efficacy compared to monotherapy, leveraging the synergistic or additive effects of different agents to combat complex diseases[4]. However, challenges such as resistance to these combinatorial therapy regimes emphasize the need for further research to optimize treatment strategies and improve patient outcomes. On the other hand, most combinations to date have been derived empirically, with limited mechanistic understanding of how multi-agent treatments interact within the cellular proteome. This limitation is particularly problematic in AML, where genetic and epigenetic heterogeneity fosters divergent responses to therapy and promotes the rapid emergence of resistant

A full list of affiliations appears at the end of the paper. e-mail: mohieddin.jafari@helsinki.fi

clones[5]. Moreover, high toxicity associated with multi-drug regimens restricts their broader clinical application and often necessitates dose reductions that compromise efficacy[6,7]. Recent work from our group addressed this challenge by systematically searching for rational AML drug combinations using a patient-derived drug–response bipartite network[8]. This approach integrates efficacy and toxicity measurements and identified two particularly promising combinations, LY3009120 with sapanisertib (LS) and ruxolitinib with ulixertinib (RU), as optimal pairs across AML patient samples, cell lines and xenografted zebrafish[9].

Proteomics-based approaches have recently emerged as promising tools for elucidating drug mechanisms of action at the systems level. One such approach is the study of drug-induced shifts in protein conformational solubility/stability, which can provide insights into the potential protein targets and then the mechanisms of action of therapeutics[10,11]. The thermal shift assays leverage the principle that drug binding affects the solubility or thermodynamic stability of a protein, allowing researchers to identify drug targets across the whole cellular proteome[12]. In a similar vein, the PISA assay is a high-throughput technique to monitor drug target engagement and has been employed to decipher the targets of hundreds of drugs recently[12–14]. However, these methods have been primarily applied to single-agent treatments and fail to capture emergent molecular effects unique to drug combinations. To overcome this gap, we developed CoPISA (Combinatorial Proteome Integral Solubility/Stability Alteration analysis), a high-throughput proteomics workflow designed to interrogate combination-specific solubility alterations in proteins.

In this work, we apply the CoPISA method to two recently identified drug combinations with demonstrated high efficacy and low toxicity in AML patient samples, cell lines, and xenografted zebrafish models[8,9]. This technique uses advanced proteomic tools to explore both primary (using lysate sample) and secondary (using living sample) target effects, providing a comprehensive understanding of how combinatorial therapies can modulate multiple signaling pathways to overcome treatment resistance[12,15]. This research extends beyond traditional drug target identification by examining how these interactions impact cellular behavior at a systems level, thereby addressing current limitations in understanding the mechanisms behind successful drug combinations. Moreover, we introduce a molecular mechanism termed 'conjunctional targeting,' where the combined action of drugs produces biological responses that are unattainable by individual compounds (more definition in the Results section). This perspective transforms our understanding of drug interactions and paves the way for more effective therapeutic strategies in AML and other complex diseases.

Results

CoPISA Assay principal and Ab Initio Simulation

To investigate how combinatorial drug treatments affect protein solubility, we used the CoPISA workflow, an extension of the PISA assay tailored for combinatorial therapies. In the CoPISA assay, we quantify protein solubility/stability by measuring the total amount of each protein, represented as the area under the melting curve of each protein (S_m), enabling precise solubility/stability measurements without the need for curve fitting. The CoPISA workflow involves treating cells with each drug individually (e.g., A and B), as well as in combination (AB), alongside untreated controls. Lysates or living cells are then subjected to thermal treatment across a temperature gradient to assess shifts in the amount of soluble/stable proteins (S_m) under each condition (Fig. 1). Relative changes in S_m compared to the control ($\triangle S_m$) provided quantitative insight into drug-induced effects on protein solubility/stability. These shifts indicate either stabilization (increased S_m) or destabilization (decreased S_m) of proteins. Note that in the following, we used "solubility" shift instead of "solubility/stability" to emphasize the change in the amount of soluble protein after altering stability with increasing temperature in the presence and absence of drugs.

Protein classes in CoPISA represent patterns of solubility-based candidate targets under specific experimental conditions (temperature range, drug concentrations, treatment time, and cell lines). These patterns do not imply definitive absence or presence of drug-target interactions, as thermal stability can be influenced by multiple factors beyond direct binding. To reduce confounding effects from PTMs and protein-protein interactions, all comparisons were made against untreated controls. Thus, the classification should be interpreted as a descriptive framework for solubility-based responses rather than a mechanistic assignment. Based on this, there are eight classes, revealing distinct impacts on protein solubility. The four trivial classes of proteins according to drug-target interactions can be hypothesized as follows: A (protein targeted by drug A), B (protein targeted by drug B), A ∩ B (protein targeted by both drug A and drug B), A∪B (protein not targeted by any drug) when using two drugs or compounds for treatment. In one class, some proteins are unaffected by all treatments, showing no changes in solubility compared to the control. Two classes involve *independent inhibition* (A or B), where treatment with either drug A or drug B alone leads to specific alterations in solubility profiles, indicating individual effects on protein solubility. These proteins could suggest a classical synergy mechanism in combinations by targeting two proteins from different or identical biochemical pathways. A ∩ B represents proteins targeted by both drug A and drug B, where combined treatment results in a distinct solubility shift, potentially indicating cooperative or enhanced binding effects. These proteins could highlight synergistic interactions where the combined action of both drugs leads to a stronger impact on solubility than either drug alone.

As a theoretical proof of principle, we conducted a simulation of melting sigmoidal curves for 10,000 hypothetical proteins to explore the possibility of all four classes. This preliminary computational analysis involved randomly selecting melting temperatures T_m in the range from 48 to 56 °C using error (erf) and square root (sqrt) functions. Examples of thus-simulated melting curves are shown in Fig. 2, illustrating the variation in thermal stability across the different protein classes. Our analysis suggests that all four expected classes of targeting proteins for this two-drug combination are theoretically possible, based on a normal distribution and hypothetical values for the mean and variance (Fig. 2A). This finding supports the idea that different classes of proteins could be differentially affected by the drug combination. In addition, we observed a similar pattern of these four classes with slightly distinct distribution based on the mean and variance values extracted from a proof-of-principle Thermal Proteome Profiling (TPP) published study[16] (Fig. 2B), further validating the robustness of our theoretical model and aligning with previously observed experimental data.

However, in the CoPISA workflow, we also consider the treatment of the combination (AB) in addition to the individual drugs. This introduces a unique condition where certain proteins are exclusively targeted by the combination treatment (AB), requiring the simultaneous presence of both drugs to induce significant shifts in solubility. We refer to this phenomenon as *conjunctional targeting (i.e., conjunctional inhibition)*, defined here as combination-specific thermal solubility/stability alteration, rather than a direct indication of functional activation or inhibition. In the specific context of this study, as all compounds are kinase inhibitors, we occasionally use the term conjunctional inhibition as a practical descriptor; however, CoPISA itself reports only solubility/stability changes and does not distinguish whether these shifts correspond to functional activation or inhibition of the affected proteins. This combinatorial effect can be framed within logical gate theory[17], suggesting a gate mechanism; both drugs must be present to induce inhibition sufficiently. This pattern indicates that these proteins may possess multiple binding sites or complex

https://doi.org/10.1038/s41467-026-70394-3

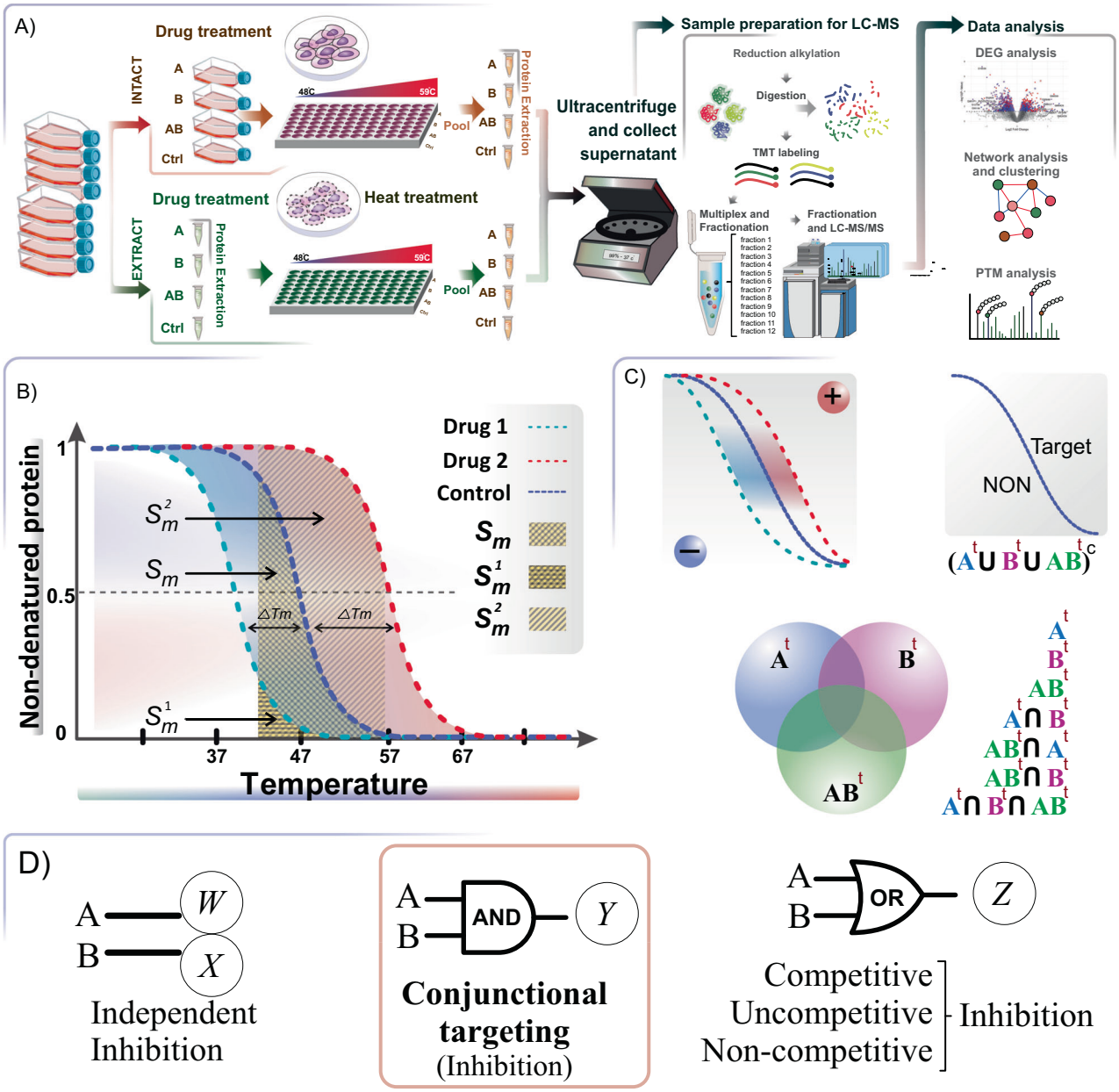

Fig. 1 | CoPISA workflow and possible states for target discovery in combinatorial therapy. A Schematic overview of the CoPISA method applied to both intact cells and lysates. Cells are treated with Drug A, Drug B, or their combination (AB) and control, followed by heat treatment across a temperature gradient (48–59 °C). Soluble proteins are isolated post-ultracentrifugation and analyzed by LC-MS, with subsequent downstream analyses. **B** Comparison of the PISA concept of integral analysis with the concept of sigmoidal curve fitting when using two drugs. In the PISA workflow, protein solubility shifts are measured based on the area under the curve ($\triangle S_m$) rather than using the median of the fitted sigmoidal curve of denatured protein ($\triangle T_m$) at several temperature points. The area under the curve for the first drug (light blue curve, S_m^1) and the second drug (red curve, S_m^2) is used to calculate $\triangle S_m$ within the temperature range of 48–59 °C. The same way is used to measure the area under the curve for the combination treatment. **C** Theoretical illustration of the CoPISA concept. This panel illustrates comparisons across multiple single treatments, including drug A, drug B, and combination AB, and various intersections of solubility-candidated targets (i.e., A^t, B^t, AB^t) of these three treatments compared to control (e.g., $AB^t \cap A^t$, $A^t \cap B^t$, $A^t \cap B^t \cap AB^t$, $AB^t \cap B^t$). It further highlights a scenario in which no target can be identified for the complement of the union of multiple treatments $\left(A^t \cup B^t \cup AB^t\right)^C$. **D** Mapping of drug inhibition models to logical gate analogies: *Independent inhibition*, where drugs A and B act separately on targets W and X, respectively, corresponds to an independent action; *conjunctional targeting*, where drugs A and B jointly affect a single target Y, aligns with the logical gate; and *competitive*, *uncompetitive*, or *non-competitive inhibition*, representing mechanisms that are either mutually exclusive or involve overlapping inhibition effects, correspond to the logical gate.

allosteric regulation modulated only by both drugs, providing insights into the underlying mechanisms of this drug combination. Conversely, if a protein is targeted in the presence of A, B, or A ∩ B, it aligns with a gate model, representing an overlap of effects across treatments. This mechanism offers an additional explanation for synergy in drug combinations, where the effects are enhanced when used in tandem compared to monotherapy.

Ultimately, we identified eight classes of proteins. Four of these classes demonstrate shared protein targets across all drug treatments ($AB^t \cap A^t$, $A^t \cap B^t$, $A^t \cap B^t \cap AB^t$, $AB^t \cap B^t$), while two classes show individual protein targets specific to drug A or B treatments. One class, termed *conjunctional targeting*, is uniquely targeted by the combination treatment (AB), and the remaining class consists of proteins that are not targeted by any treatment.

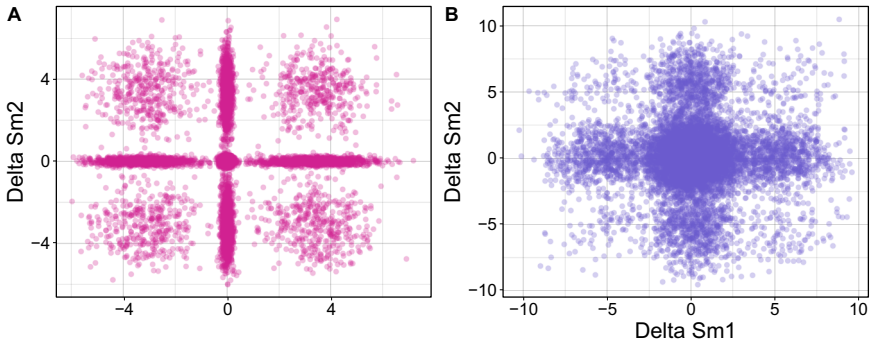

Fig. 2 | The simulated relationship of protein thermal shift of two hypothetical drugs. A $\triangle S_m^1$ and $\triangle S_m^2$ in 10,000 proteins were simulated and depicted using a normal distribution with hypothetical mean and variance, and (**B**) with mean and variance extracted from the proof-of-principle TPP published article[16]. Source data are provided as a Source Data File.

Global CoPISA Profiling and Intersectional Target Analysis in AML Cell Lines

We applied the CoPISA workflow to four AML cell lines, MOLM-13, MOLM-16, SKM, and NOMO-1, to examine how each single agent (LY3009120, sapanisertib, ruxolitinib, and ulixertinib) and its corresponding combination (LS and RU) reshape the soluble proteome. Both lysates (capturing direct, primary binding events) and intact cells (capturing the net effect of primary and secondary interactions) were analyzed.

Volcano plots (Fig. 3A–D) illustrate a striking yet therapy-specific redistribution of protein solubility. In the living cell condition (Fig. 3A), treatment with ruxolitinib, ulixertinib, and the RU combination resulted in 334, 393, and 553 significantly altered proteins, respectively. In the lysate (Fig. 3B), treatment with ruxolitinib, ulixertinib, and the RU combination yielded 350, 479, and 146 significantly altered proteins, respectively. Corresponding to intact or living cells (Fig. 3C), treatments with LY3009120, sapanisertib, and the LS combination yielded 349, 293, and 308 significantly altered proteins, respectively. The cell lysates treated with LY3009120, sapanisertib, and the LS combination resulted in 270, 141, and 215 significantly altered proteins, respectively (Fig. 3D, Source Data File). These findings highlight that, while individual treatments tend to produce extensive alterations in protein solubility, the combination treatment exhibits a more selective pattern of solubility changes, particularly under the lysate condition. Together, these observations underscore the differential impact of single and combined treatments on protein solubility, with notable differences between lysate and living cell conditions that may inform the distinct mechanistic effects of combinatorial therapies on protein dynamics.

To ensure the robustness of the significance cutoff and to effectively control the false discovery rate (FDR) for solubility shifts, a comprehensive permutation analysis of protein S_m values was conducted. The analysis demonstrated that, on average, the FDR across all twelve comparison analyses was maintained at 5.25% for 12000 permutations, ensuring the reliability of the identified significant solubility shifts. Taken together, these data show that each regimen reshapes the AML proteome in a unique and context-dependent manner.

To determine how consistently the two drug pairs engage their intracellular targets, we compared proteins whose solubility was significantly altered in lysate-based (primary targets) and intact-cell (primary + secondary targets) CoPISA experiments (Fig. 4). Across all treatments, the living-cell fractions yielded more hits than lysate samples, as expected from the metabolic activity of intact cells and the capture of both primary and secondary protein targets. Notably, the LY3009120–sapanisertib (LS) combination shifted the solubility of 177 proteins in living cells but only 147 in lysate; ruxolitinib–ulixertinib (RU) affected 414 and 89 proteins, respectively. These partially overlapping target sets point to distinct intracellular consequences of the two regimens.

Importantly, there are some proteins that are targeted only in single treatment, not in combination, suggesting that certain drug-specific interactions may be masked or modulated during co-treatment, potentially reflecting competitive binding, pathway redundancy, or negative crosstalk that diminishes individual drug effects when used in combination.

In Fig. 4, the CoPISA approach was used to compare drug-dependent target engagement between living cells and cell lysates. Each Venn diagram shows the distribution of targets unique to living cells, unique to lysates, and shared between both. While most targets were condition-specific, a notable number of overlapping proteins, particularly in the Ruxolitinib (25), Ulixertinib (43), and combination treatments (13 each), serve as a strong validation of the CoPISA method across these distinct experimental conditions. These shared targets reflect consistent drug-protein interactions detectable in both intact and lysed cellular environments, supporting the robustness of CoPISA in mapping solubility shifts associated with drug binding.

In samples treated with LY3009120, 20 proteins with significant solubility shifts are consistently detected in both living cells and cell lysate samples (Fig. 4). Among these, PTPN11, encoding the SHP2 phosphatase frequently mutated in myeloid malignancies, suggests inhibition of RAS/MAPK pathway signaling critical for leukemic cell maintenance[18]. In sapanisertib-treated samples, 10 proteins are shared between lysate and intact cell conditions. Notably, S100A8, a calcium-binding protein implicated in inflammatory signaling and leukemogenesis, suggests a role for sapanisertib in modulating immune-related pathways[19]. Other intersected proteins, such as UCHL1 and TPM1, suggest modulation of protein turnover and cytoskeletal dynamics, respectively, which may influence AML cell viability[20,21]. Under the combination-treated samples, 13 proteins are shared in lysed and intact samples, while under the AND gate, seven proteins are targeted in samples treated with the combination of LS in both living cell and lysate samples. Among these, ICAM3, an adhesion molecule, suggests effects on leukemic cell adhesion and trafficking within the bone marrow niche[22]. Collectively, these findings support the hypothesis that the LS combination elicits conjunctional targeting through combinatorial targeting of signaling, adhesion, and trafficking mechanisms.

In the ruxolitinib-treated samples, 25 proteins are targeted in both living cell and lysate samples (Fig. 4). Of particular note, ABL1, a non-receptor tyrosine kinase, plays critical roles in leukemogenesis and resistance to therapy, suggesting that ruxolitinib may suppress oncogenic kinase signaling in AML[23]. Similarly, in ulixertinib-treated samples, 45 proteins were shared between lysate and living cell conditions. The detection of MAPK3 (ERK1), a central node in the MAPK pathway,

https://doi.org/10.1038/s41467-026-70394-3

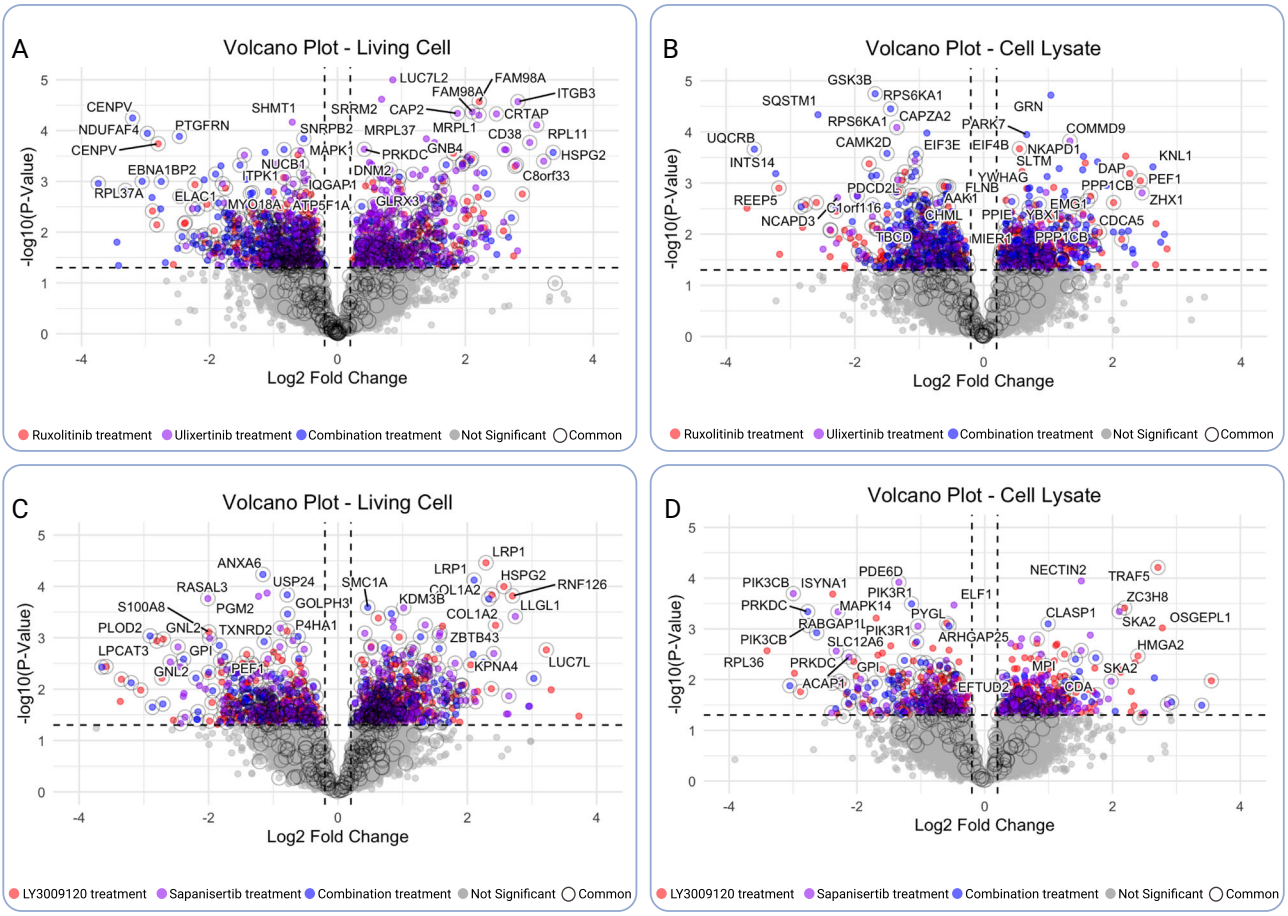

Fig. 3 | Volcano plots reveal protein targets identified by the CoPISA method in lysate and living cell treatments with drug combinations. Each panel is a superimposition of three comparisons between control and treatment groups, with solubility shifts indicated by different colors: living cells (**A**) and lysate cell samples (**B**) treated with ruxolitinib (3 uM) (red), ulixertinib (3 uM) (blue), and their combination, RU (purple); and living cells (**C**) and lysate cell samples (**D**) treated with LY3009120 (500 nM) (red), sapanisertib (500 nM) (blue), and their combination, LS (purple). Dots with outlines represent proteins uniquely identified in the corresponding treatment. Statistical significance was assessed using linear models with empirical Bayes moderation implemented in the limma framework. For each comparison, moderated two-sided t-tests were performed comparing treatment versus control. Volcano plots are presented using log10-transformed P-values and log2-transformed fold changes. To provide a reliable assessment of statistical significance, we estimated false discovery rates using a permutation-based approach (see "Methods"). Source data are provided as a Source Data File.

underscores inhibition of proliferative signaling cascades by ulixertinib[24]. Under the combination treatment, 13 proteins are shared in lysate and intact samples, and four proteins are specific to the combination and are not targeted in single treatment. TTC19, a mitochondrial protein involved in respiratory chain complex III assembly, suggests that RU combinatorial therapy may compromise mitochondrial bioenergetics, leading to enhanced apoptotic priming of AML cells[25]. These conjunctional targets reinforce the concept that RU combinatorial therapy reprograms key cellular processes to induce synthetic lethality in leukemic cells.

Taken together, these updated intersectional analyses provide deeper insight into how single and combination treatments differentially engage cellular targets in AML, with the AND-gate proteins emerging as critical effectors of combinatorial synergy. These findings highlight therapeutic vulnerabilities that could inform the rational design of precision-guided combinatorial regimens.

To further investigate the association patterns in protein solubility alterations induced by combination treatments, we generated fold change-fold change (FCFC) plots (Fig. 5). These plots compare the solubility alterations in proteins for each combination treatment relative to the effects observed with the individual drugs alone. Specifically, the FC-FC analysis examines (1) combination vs. drug 1 (e.g., LS combination vs. LY3009120 alone) and (2) combination vs. drug 2 (e.g., LS combination vs. sapanisertib alone). Notably, we observed multiple concordant proteins shared between the volcano plots and different FC–FC plots (Fig. 5). For example, SMC1A, a cohesin complex component involved in chromatin organization and cell-cycle control, was consistently identified as a common target, appearing as a significant hit in the LS volcano plots (Fig. 3). Interestingly, only 0.84% of protein alterations exhibit inconsistent directional changes, where stabilization or destabilization patterns differ between combination and single-drug treatments. This finding highlights a strong alignment between the solubility alteration patterns induced by the combination treatments and those observed for individual drugs, particularly from a stabilization perspective. These results reinforce the idea that combination treatments largely maintain the stabilization directionality of the single drugs, providing further evidence of their targeted and coordinated action on protein solubility.

To further contextualize and validate the CoPISA findings, we examined whether proteins significantly altered by drug treatments corresponded to known targets of the respective agents (DrugBank and TTD). Several expected primary targets were detected: PLAUR for ruxolitinib, MAPK1 and MAPK3 for ulixertinib, and ARAF for LY3009120. These results demonstrate that CoPISA can detect both direct drug targets and proteins reflecting broader mechanistic responses, supporting its specificity and utility for interrogating

https://doi.org/10.1038/s41467-026-70394-3

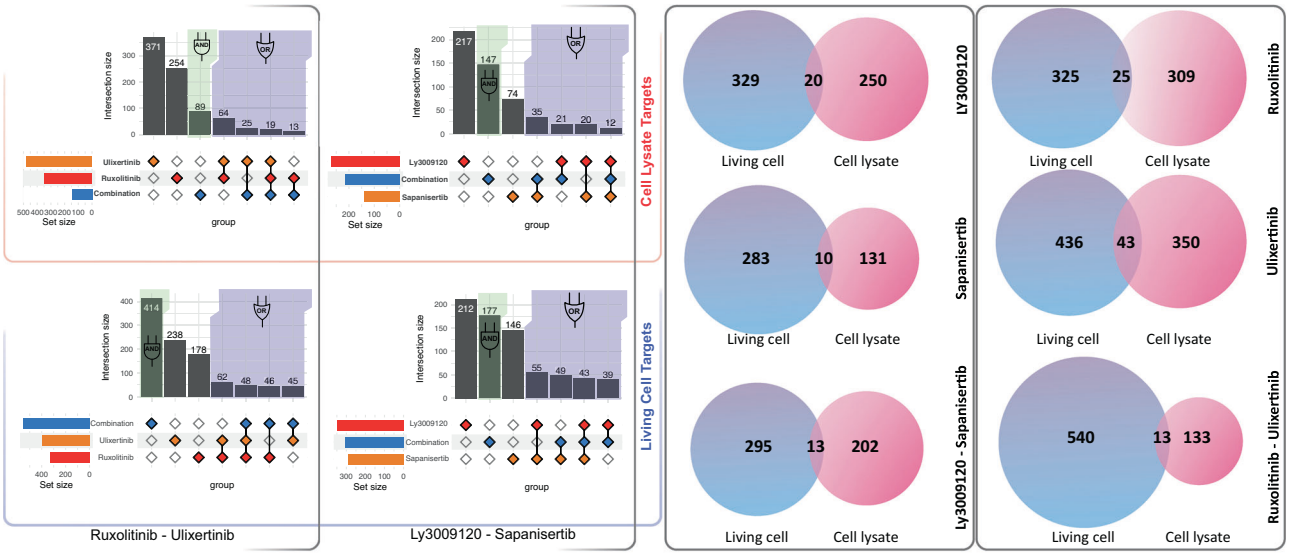

Fig. 4 | Comparison of protein targets identified in lysates and living cells across drug treatments. UpSet plots show the number of protein targets identified in lysate and living cell samples following treatment with LY3009120–sapanisertib and ruxolitinib–ulixertinib. Venn diagrams further illustrate the distribution of targets detected using the CoPISA method across both sample types–living cells and lysates–after treatment with individual drugs and their combinations. In each diagram, targets unique to living cells are shown in blue, those unique to lysates in pink, and shared targets in the purple overlap region. These visualizations provide insights into drug-dependent protein interactions under different cellular conditions. Source data are provided as a Source Data File.

single-agent and combination drug effects at a proteome-wide scale.

Exploring drug-drug interactions through mass spectrometry analysis

In the next phase, potential noncovalent interactions or unforeseen reactions within the selected drug combinations were examined to ensure that the observed effects on protein solubility were independent and specific to each compound. Using LC-MS/MS analysis[26], we compared the spectral profiles of each drug alone with those of the combined samples (Fig. 6). By analyzing the MS1 spectra and extracted ion chromatograms (XICs) of each compound separately and in combination, we assessed whether a new profile emerges from reacting or interacting drug molecules.

The XICs and MS1 spectra of the combined drugs showed no other peaks or mass shifts other than initial single-drug ion peaks, indicating an absence of detectable interactions or reactions between the compounds or their modification. In addition, cosine similarity analysis of the whole MS1 spectra provided a comparative view of each drug combination. This analysis confirmed that the effects observed on protein targets were attributable to specific mechanisms of each drug, rather than nonspecific interactions within the combinations. Each compound displayed stable peak intensities and retention times across conditions.

These findings support the hypothesis that the protein targets identified for the LS and RU combinations arise from the concurrent, yet independent, actions of each drug, rather than from non-specific interactions between them. This reinforces the proposed "AND gate" inhibition mechanism in combinatorial therapy, suggesting these combinations achieve synergistic effects through coordinated drug action and potential engagement of signaling pathways.

Mechanistic Insights into "AND" and "OR" Gate Targeting Patterns

To gain deeper insight into the mechanisms underlying the drug combinations, we performed comparative pathway enrichment analysis of proteins exhibiting significant solubility shifts in response to LS and RU treatments. These analyses leveraged both lysate and intact cell fractions to distinguish context-specific biological processes perturbed under combinatorial treatment. The framework of "AND" and "OR" logic gates allowed us to differentiate between synergistic effects of combinatorial therapies, i.e., independent or conjunctional targeting (Fig. 7, Source Data File). This systems-level approach uncovered molecular signatures that converge on key vulnerabilities in AML biology.

Within the "AND" gate, representing proteins selectively responsive to the LS combination but not either single agent, significant enrichment is observed in SUMOylation processes as primary targets (Fig. 7A). This points to disruption of genome stability and transcriptional control pathways, which are critical for leukemic maintenance and progression[27]. Enrichment of mitotic phase processes, including chromatin condensation and nuclear envelope dynamics, further indicates interference with cell division fidelity, a hallmark vulnerability in rapidly proliferating AML cells[28]. Conversely, enrichment analysis of proteins from living cell samples, which represents downstream pathways beside direct targets, highlights RNA processing and immune function. These findings suggest that the combination treatment predominantly interferes with transcriptional output and modifies immune interactions within the AML microenvironment[29]. Proteins shared across lysate and living cell fractions under the "AND" gate configuration reveal additional points of vulnerability. These include activation of stress-responsive transcription, redox homeostasis, metabolic rewiring, lipid signaling, and immune remodeling. Disruption of WNT signaling and CD209-mediated pathways further implicates LS in undermining both developmental and innate immune axes, processes increasingly linked to AML cell persistence and therapy resistance[30,31]. These converging effects underscore a multi-axis destabilization of AML cell resilience.

Further analysis of the "OR gate" under LS treatment reveals distinct yet interconnected patterns between lysate and living cells (Fig. 7B). Lysate-specific proteins prominently involve mitogenic and growth factor signaling cascades, particularly receptor tyrosine kinase-driven (RTKs) pathways, emphasizing interference with key proliferative and metabolic regulatory circuits. Targeting these pathways is crucial, as RTK-driven signaling often sustains leukemic growth and survival, making their inhibition a promising therapeutic approach in

https://doi.org/10.1038/s41467-026-70394-3

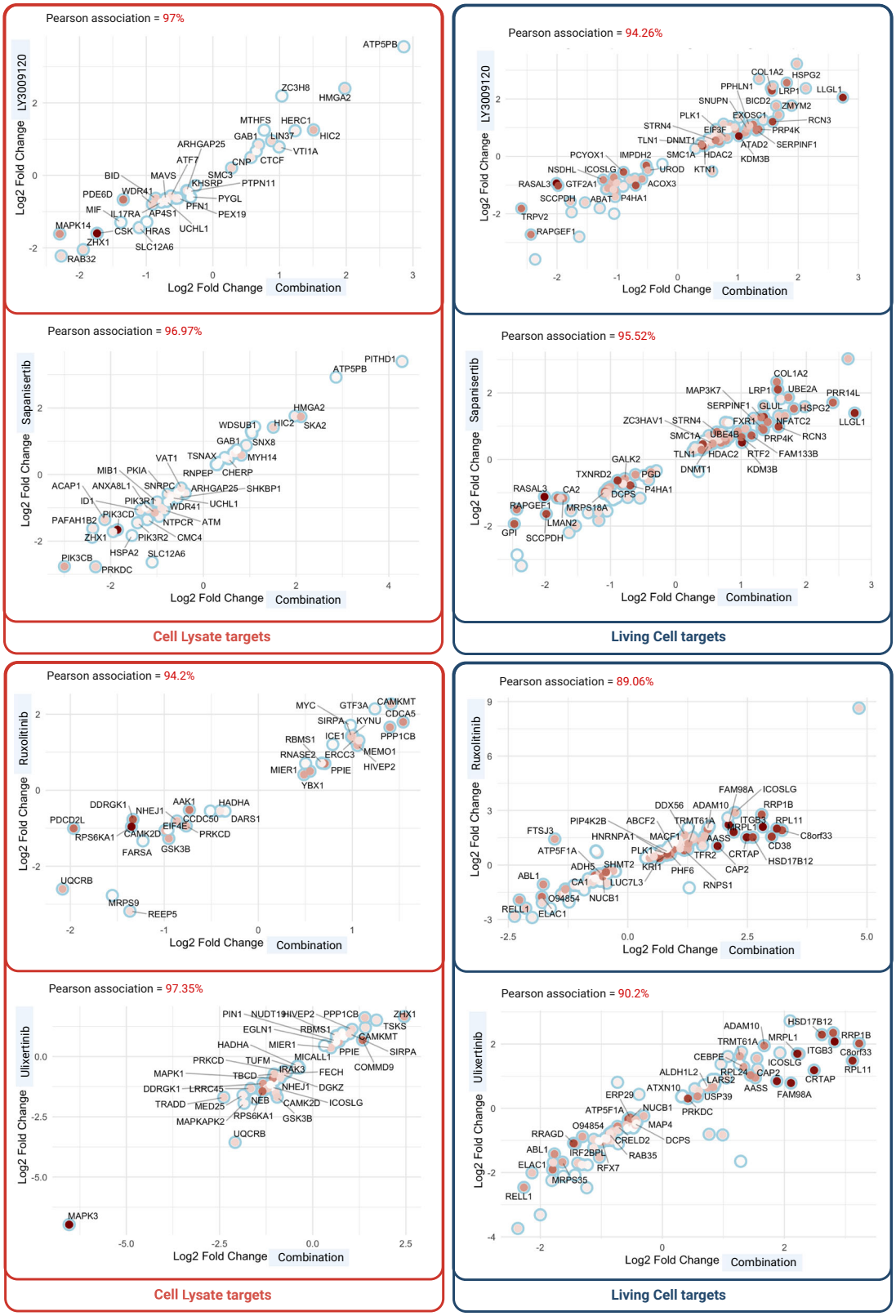

Fig. 5 | Pairwise fold change comparisons of treatment conditions based on significant protein targets. The FC-FC plots display common protein target IDs with fold change values for each treatment relative to control samples. These plots are presented separately for cell lysate (red frame left panels) and living cells (dark blue frame right panels), with distinct panels for each combination. Dot color represents p-values ranging from 0.05 to 0, with lighter shades indicating higher p-values and darker brown indicating lower *p*-values. Source data are provided as a Source Data File.

https://doi.org/10.1038/s41467-026-70394-3

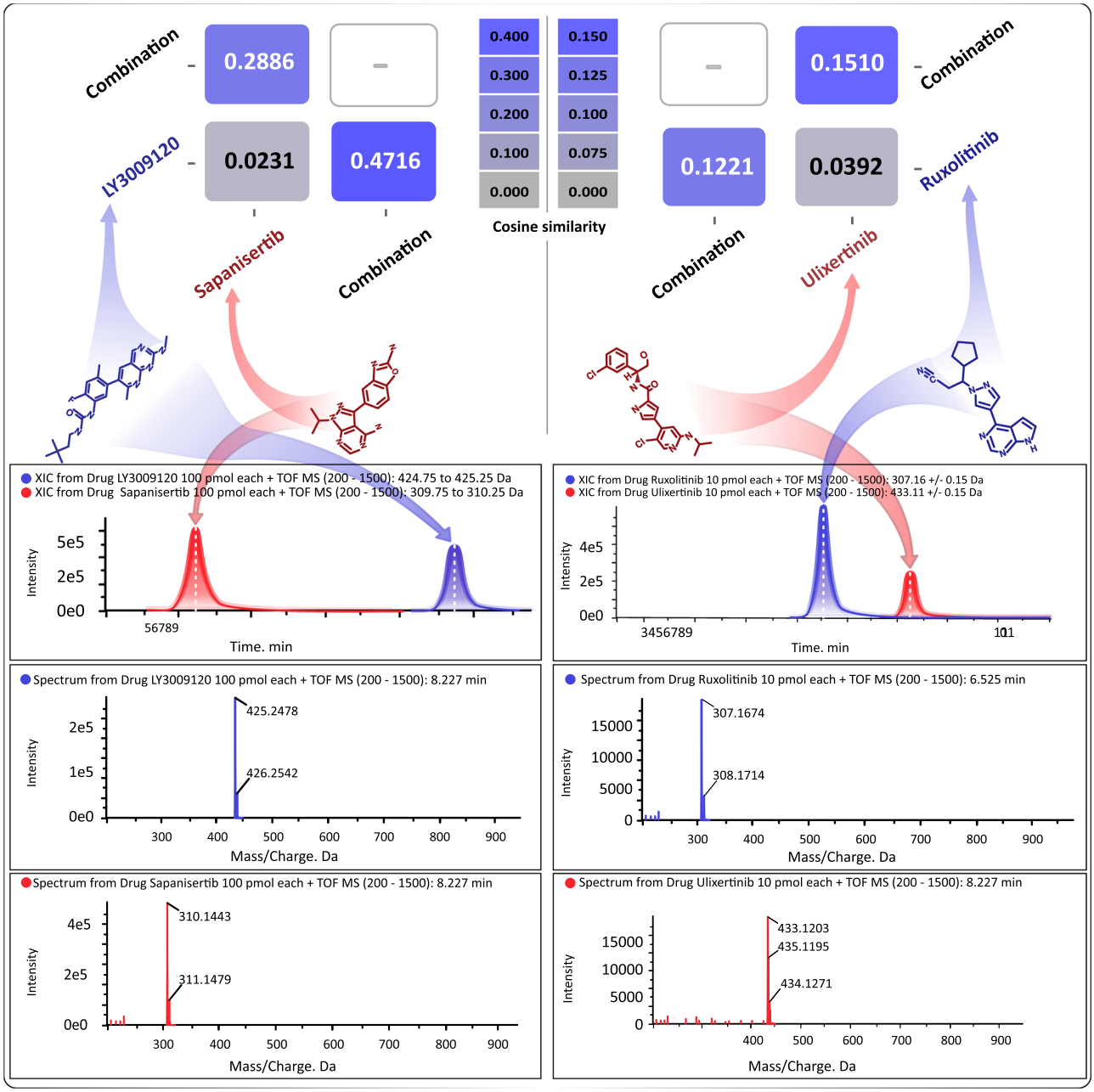

Fig. 6 | Mass spectrometry analysis of four individual compounds and their combinations. Molecular structures of each compound are shown alongside their MS1 spectra and total ion currents (TICs) for the combined drug samples. For each drug combination, TIC plots are provided to display the corresponding chromatographic profiles and detected mass-to-charge (m/z) values for each compound. Pairwise cosine similarity of TICs between individual compounds and their combinations is presented based on quantified MS peak intensities.

AML[32]. In contrast, living cell-specific pathways are heavily enriched in translation and protein homeostasis mechanisms, implicating significant disruptions to ribosome assembly, protein synthesis, and mRNA surveillance. This reflects suppression of biosynthetic output and stress-induced translational reprogramming, which AML cells rely on to sustain high proliferative demands and evade treatment stress[33]. Importantly, shared targets between both fractions, although fewer in number, converge on critical biosynthetic processes, including phospholipid metabolism and RNA splicing. These pathways govern membrane integrity and transcriptome regulation, and their coordinated disruption may destabilize intracellular architecture and gene expression fidelity. Altogether, the OR-gate analysis reveals how LS imposes widespread molecular pressure by targeting essential survival signaling, metabolic infrastructure, and RNA regulatory mechanisms, driving cumulative cellular stress that likely exceeds the adaptive capacity of AML cells.

In parallel, the RU combination demonstrates complementary mechanistic patterns (Fig. 7C). The “AND” gate analysis for RU identifies lysate-specific enrichment in transcriptional regulation, cell cycle control, apoptosis, and epigenetic modulation, which reflect primary disruption of proliferative signaling and tumor suppressor networks frequently dysregulated in AML[34]. Living cell-specific pathways emphasize translation control and protein homeostasis, indicating significant disruptions to ribosome assembly, protein synthesis, and mRNA surveillance, pathways crucial for maintaining the high biosynthetic and metabolic demands of AML cells[35]. Shared targets in both fractions consistently impact phospholipid metabolism and RNA splicing, underscoring a unified effect on fundamental biosynthetic

https://doi.org/10.1038/s41467-026-70394-3

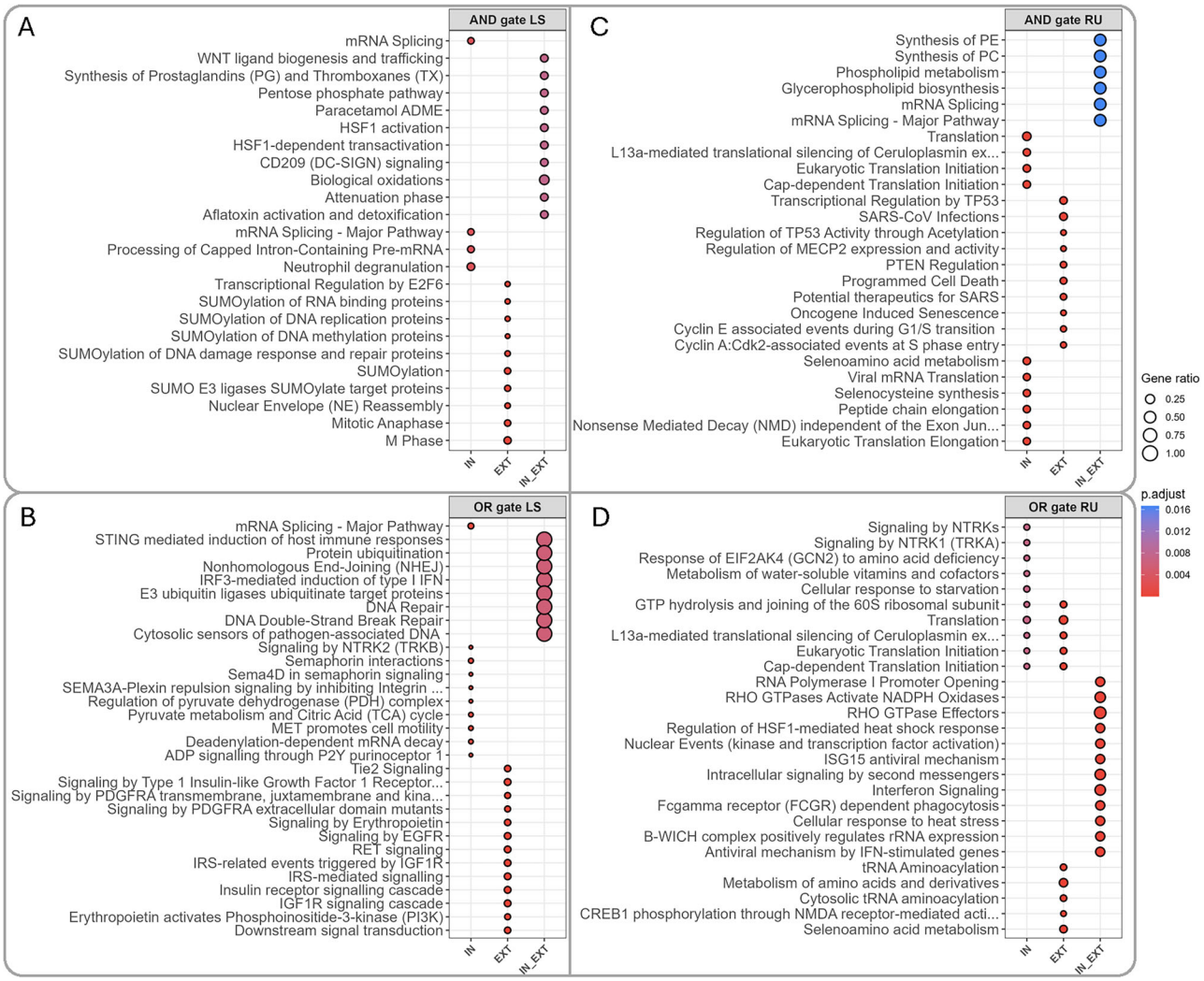

Fig. 7 | Bubble plots illustrating the top enriched Reactome pathways (p.adj < 0.05) for each combination and gating logic. The top enriched pathways are shown for LS and RU combinations, as well as AND- and OR-gate targets, in these panels. Panel (**A**) shows the AND-gate (conjunction) results for LY3009120 and sapanisertib; panel (**B**) shows the OR-gate (disjunction) results for the same combination. Panel (**C**) shows the AND-gate results for ruxolitinib and ulixertinib, while panel (**D**) shows the OR-gate results for this combination. Within each panel, bubbles at "IN" represent pathways unique to intact (live) samples, "EXT" indicates pathways unique to extract (lysate) samples, and "IN_EXT" identifies pathways common to both. Bubble size corresponds to gene ratio (pathway genes / total tested), and color intensity reflects raw p-values (red = lower, blue = higher). Pathway names are truncated for clarity. Pathway enrichment analysis was performed using ReactomePA based on over-representation analysis. *P*-values were adjusted for multiple testing using the Benjamini–Hochberg method, and pathways with adjusted $P < 0.05$ were considered significant. Source data are provided as a Source Data File.

processes fundamental for AML cell integrity and proliferation[36]. These findings highlight the ability of RU to inhibit biosynthetic machinery critical for AML cell survival and proliferation.

Similarly, OR-gate analysis of RU drug combination treatment across lysate and intact cell fractions identifies extensive disruptions in translational control and stress response pathways that are critically relevant to AML pathobiology (Fig. 7D). Lysate samples emphasize modulation of protein biosynthesis, amino acid metabolism, and transcriptional regulation, core processes that are often upregulated in AML to support unchecked proliferation and metabolic adaptation[31]. In the intact cells, RU highlights interference with translation initiation and metabolic stress sensing, which are essential for AML cells to withstand nutrient limitation and therapeutic pressure[37]. Shared proteins underscore activation of innate immunity and redox regulation, processes that are increasingly recognized for their role in AML immune evasion and oxidative stress tolerance[30]. These convergent mechanisms suggest that RU therapy disrupts not only biosynthetic and metabolic robustness but also immunomodulatory axes, delivering a comprehensive blockade of AML cellular resilience and survival.

In conclusion, comparative "AND" and "OR" gate analyses highlight how LS and RU combinations distinctly yet convergently target AML vulnerabilities. LS primarily disrupts proliferative signaling and metabolic regulation, with secondary effects on RNA processing and immune modulation. Shared vulnerabilities under LS include phospholipid metabolism, redox balance, and RNA splicing, collectively destabilizing AML cell survival networks. Similarly, RU primarily impairs translational control and stress response pathways, with secondary disruption of immune regulation and biosynthetic processes. Shared targets for RU converge on phospholipid metabolism and RNA processing, undermining AML biosynthetic and adaptive capacity. These findings illuminate critical molecular nodes and provide a mechanistic rationale for designing combinatorial therapies to overcome resistance and improve AML outcomes.

Roles of CoPISA-Identified Protein Targets in AML-Associated Signaling Networks

We performed a comprehensive functional interaction network analysis of AML-associated proteins to better understand the mechanistic implications of the combinatorial therapies LY3009120-sapanisertib (LS) and ruxolitinib-ulixertinib (RU). The AML-associated network is constructed by integrating Reactome signaling interaction data with high-confidence AML-associated genes derived from DepMap[38] and the mutation dataset of the FIMM-AML cohort study ($p < 0.001$, high-impact variants)[39]. Directed shortest paths connecting AML-associated protein pairs result in a robust subnetwork containing interconnected components reflective of critical AML biology.

To distinguish treatment-specific perturbations within the AML network, we quantified the overlaps of AML subnetwork genes modulated by each combinatorial regimen (Supplementary Fig. 1). This comparative analysis reveals that LS treatment modulates a total of 43 AML-associated genes, with 18 genes (42%) uniquely targeted by this combination and not by either single drug. This relatively high proportion of combination-specific targets underscores the synergistic potential of LS to engage molecular vulnerabilities that remain inaccessible to monotherapies. Similarly, RU treatment perturbs 49 AML-associated genes overall, of which 22 genes (45%) are distinct to RU, further highlighting the capacity of this combination to reprogram AML-specific networks in a manner that extends beyond the additive effects of its individual components. These findings indicate that both LS and RU elicit a substantial degree of unique network rewiring, suggesting they engage complementary biological processes and may overcome redundant survival pathways exploited by leukemic cells under single-agent treatment.

Building on this annotated, treatment-layered AML subnetwork, we applied community detection, identifying 44 discrete clusters. Seventeen clusters (i.e., C3, C4, C6, C8, C9, C11, C12, C14, C16, C19, C22, C24, C28, C29, C32, C36, and C38), prioritized based on a size threshold (≥ 15 genes) and overlap with CoPISA solubility shifts, were annotated using Reactome over-representation analysis (FDR ≤ 0.05). These clusters represent functional modules ranging from epigenetic regulation to immune signaling, offering a systems-level view of therapy-induced vulnerabilities (Fig. 8A, Source Data File).

The prioritized clusters highlight distinct processes significantly enriched within the AML network context, reflecting both shared and unique vulnerabilities to LS and RU treatment (Fig. 8B). A prominent set of clusters (C32 and C29) highlights extracellular and microenvironmental dependencies, including extensive enrichment for ECM organization and remodeling, integrin-mediated adhesion, gap junction turnover, Rho GTPase–regulated cytoskeletal dynamics, and VEGFA–VEGFR2 signaling. These pathways reflect key interactions between leukemic blasts and the bone marrow niche, supporting survival, migration, and metabolic stability, processes that are increasingly recognized as critical mediators of therapy resistance in AML (Fig. 8C, Source Data File)[40].

A second major group of clusters (C28, C24, and C22) reveals extensive enrichment of immune-modulatory and stress-adaptive pathways. LS and RU targeted proteins affect BCR- and FcγR-dependent signaling, DAP12-mediated phagocytosis, PD-1 checkpoint signaling, TCR activation, and MHC class II antigen presentation, reflecting the capacity of these combinations to perturb AML-driven immune evasion[41]. Complementary enrichment of oxidative stress adaptation (KEAP1–NFE2L2), neddylation, and other post-translational modification systems underscores therapeutic disruption of AML's stress-buffering networks. These processes are crucial for leukemic resistance to apoptosis and inflammatory stress, and their appearance among the treatment-targeted proteins emphasizes LS and RU's ability to dismantle non-oncogene addiction programs central to AML survival (Fig. 8C, Source Data File)[42].

The most prominent intracellular modules (C19, C16, C14, C12) capture fundamental vulnerabilities in cell-cycle control, chromatin regulation, TP53 signaling, and cell death pathways. Targeted proteins within these clusters map to mitotic spindle assembly, sister chromatid separation, and checkpoint control, as well as epigenetic modifiers, chromatin organizing factors, and SUMOylation pathways, all of which are recurrently altered in AML to maintain high proliferative output and transcriptional plasticity. C14 demonstrates strong enrichment for apoptosis, pyroptosis, and regulated necrosis, indicating that LS and RU combinations activate or expose cell death circuits typically suppressed in AML blasts. Cluster C12 further highlights direct targeting of the PI3K/AKT axis, PTEN regulation, and secondary messenger signaling, supporting the known importance of PI3K/AKT-driven metabolic and survival programs in AML and reinforcing the rational basis for dual-pathway targeting.

Additional enriched clusters (C11, C9, C8) map to DNA damage repair, G1/S and G2/M progression, replication stress response, Rho GTPase cycling, and inflammatory signaling. These pathways represent hallmark vulnerabilities of AML, which is characterized by high replication stress, checkpoint dysregulation, and aberrant cytoskeletal organization[43]. Finally, developmental and oncogenic driver clusters (C6, C4, C3) reveal targeted perturbation of HOX gene activation, RUNX1- and E2F6-mediated transcription, centrosome maturation, and core signaling circuits including FLT3, MAPK, interleukin, and PI3K/AKT networks. These transcriptional programs form the backbone of AML stemness, differentiation blockade, and proliferative signaling, and their appearance among the LS and RU targeted Reactome terms underscores the combinations' capacity to disrupt oncogenic circuitry at multiple hierarchical levels. Together, the Reactome enrichment patterns demonstrate that LS and RU combinations each engage distinct AML vulnerabilities. The targeted proteins map to microenvironmental adhesion and ECM remodeling, immune and stress adaptation pathways, chromatin regulatory mechanisms, mitotic and checkpoint fidelity, PI3K/AKT survival signaling, and multiple programmed cell-death routes. By converging on these modules, many of which are not efficiently perturbed by single agents, LS and RU achieve deeper and broader network disruption, supporting their potential to overcome compensatory signaling and target core leukemic dependencies.

To further focus the molecular effects of combination-specific potential targets, we filtered enrichment terms in which there are genes targeted by each combination. For the LS regimen, we isolated 13 genes exclusively modulated by LS, which are in multiple clusters and involved in different Reactome pathways (Fig. 9A). Cluster 11 contributes the largest fraction of these LS-specific hits, encompassing key chromatin and epigenetic regulators such as RBBP7, DNMT3A, and RING1. These proteins are enriched in pathways including transcriptional regulation by E2F6, epigenetic regulation of gene expression, chromatin organization, SUMOylation of DNA methylation proteins, and defective pyroptosis, highlighting LS's capacity to perturb chromatin dynamics, transcriptional control, and cell death programs central to AML survival.

Cluster 16 contains additional LS-specific targets such as BRCA1, ASH2L, and CNOT3, which are involved in TP53-regulated transcription, chromatin modification, SUMOylation, and WNT signaling. This combination of intracellular signaling and epigenetic modulation suggests that LS may compromise AML cell cycle regulation and stress response pathways, thereby sensitizing cells to apoptosis.

Clusters 3, 8, and 9 highlight LS-specific engagement of signaling and structural networks. In cluster 3, ARAF is implicated in MAPK1/MAPK3 signaling, RAF/MAP kinase cascades, and broader diseases of signal transduction. Hyperactivation of *MAPK1/MAPK3* is a hallmark of AML, transmitting growth factor and cytokine cues to support leukemic cell expansion and therapy resistance[44], so targeting this protein

https://doi.org/10.1038/s41467-026-70394-3

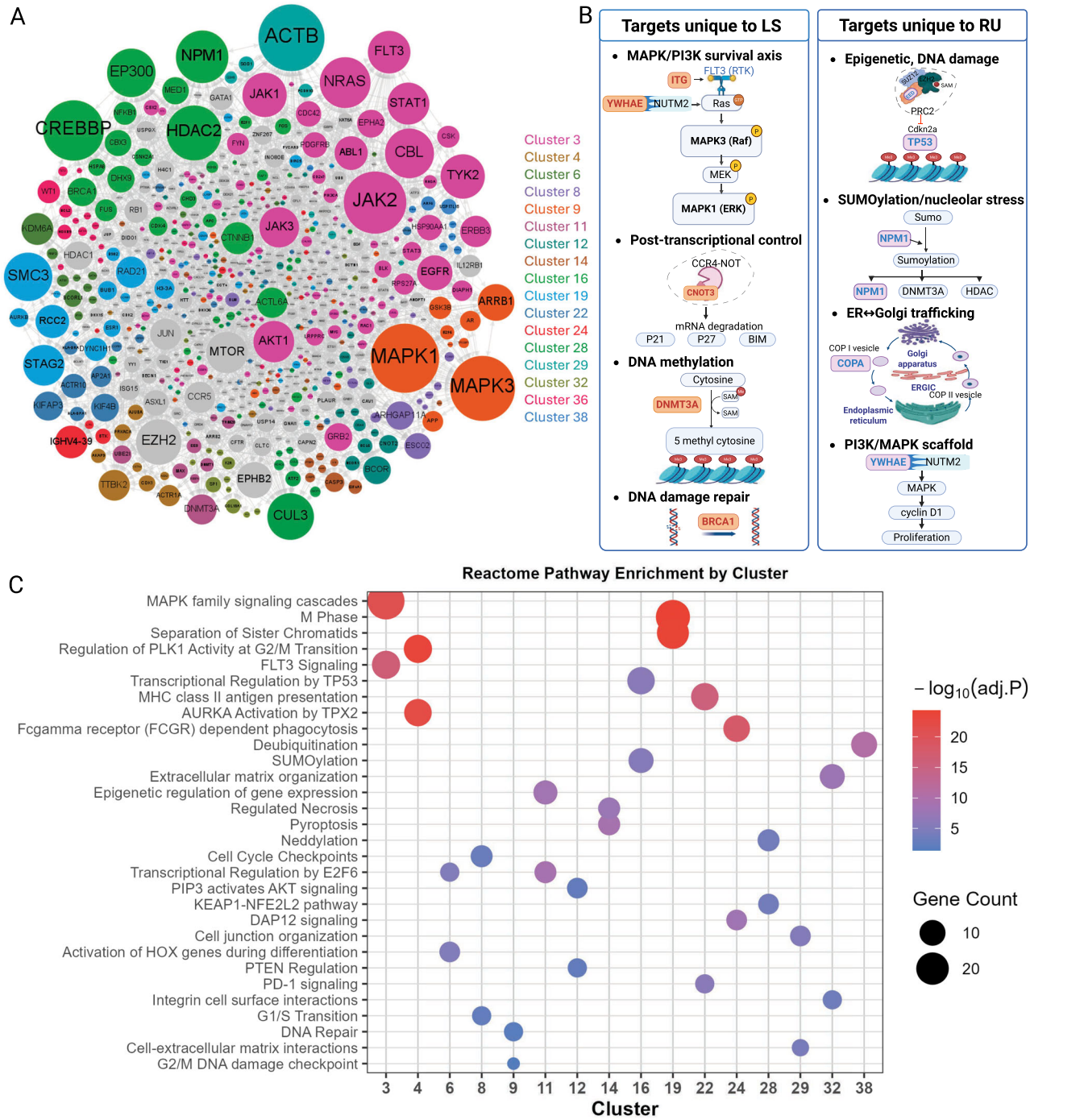

Fig. 8 | Functional interaction network of AML-associated genes revealing key proteins and pathways targeted by LS and RU combinatorial therapies. A The network was constructed by integrating Reactome signaling interactions with high-confidence AML-associated genes derived from DepMap and the mutation data of the FIMM-AML cohort study ($p < 0.001$, high-impact variants). Directed shortest paths between all AML-associated protein pairs were used to define an induced subnetwork. Community detection using the Infomap algorithm identified 44 discrete clusters. Clusters with ≥15 genes overlapping CoPISA solubility shifts are highlighted in color. **B** Key AML-related proteins significantly altered by LS or RU, as detected by CoPISA solubility shifts, are highlighted, illustrating treatment-specific perturbations across the network. Created in BioRender. Gholizadeh, E. (2026) BioRender.com/mxrji5o (**C**) Each cluster is annotated via Reactome pathway enrichment (p.adj < 0.05), highlighting distinct functional modules. For clarity, two representative umbrella pathways per cluster are shown, capturing the dominant biological themes. *P*-values were adjusted for multiple testing using the Benjamini–Hochberg method. Pathways with adjusted $P < 0.05$ were considered significant. Source data are provided as a Source Data File.

is highly effective in AML treatment. Cluster 8 contains TPX2, a regulator of TP53 activity, indicating modulation of tumor suppressor signaling. Cluster 9 genes like ABI1 are enriched for actin dynamics and phagocytic cup formation, suggesting effects on cytoskeletal remodeling and microenvironmental interactions.

Clusters 14, 29, and 32 highlight LS-specific targeting of apoptosis and extracellular matrix pathways. YWHAE, in cluster 14, modulates intrinsic apoptosis pathways, while CTTN in cluster 29 influences RHO GTPase signaling and cytoskeletal organization. Cluster 32 includes THBS1 and ITGA5, which regulate extracellular matrix organization and

https://doi.org/10.1038/s41467-026-70394-3

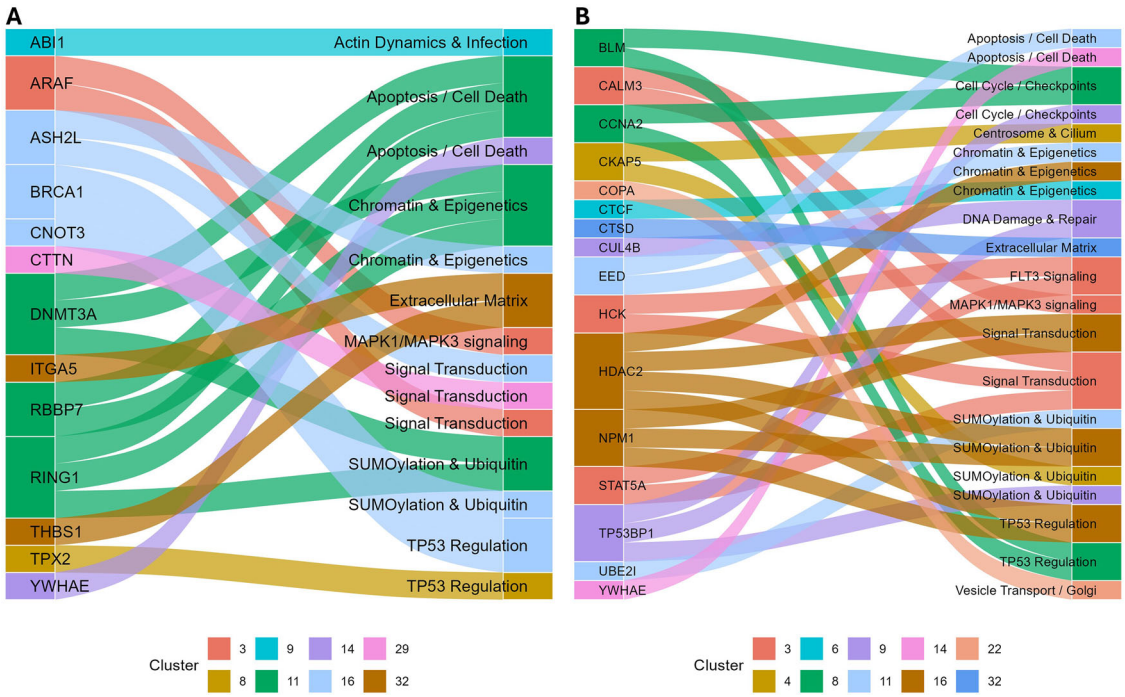

Fig. 9 | Pathway enrichment for LS- and RU-specific AML genes. A LS-specific genes: The Sankey plot (left) shows unique LS cluster genes (left nodes) and their associated enriched pathways (right nodes), with flows colored by cluster assignment. **B** RU-specific genes: The Sankey plot (left) shows unique RU cluster genes (left nodes) and their associated enriched pathways (right nodes), with flows colored by cluster assignment. Source data are provided as a Source Data File.

integrin cell surface interactions, pointing to LS's potential to disrupt AML–microenvironment interactions that support leukemic cell survival and migration.

Together, these LS-exclusive proteins converge on multiple critical AML vulnerabilities: epigenetic regulation, TP53-dependent transcriptional control, MAPK signaling, cytoskeletal dynamics, apoptosis, and niche interactions. The Reactome pathway enrichment emphasizes the multifaceted nature of LS-specific network rewiring, demonstrating the combination's potential to engage non-overlapping molecular dependencies that are not efficiently targeted by single-agent therapies.

By filtering our prioritized clusters for those genes uniquely modulated by RU, we isolated 16 RU-exclusive targets spanning multiple clusters (Fig. 9B), and these genes unmask combination-specific mechanisms. Cluster 3 contributes the largest fraction of these RU-specific hits, including CALM3, STAT5A, and HCK, which map to key signal transduction and FLT3signaling pathways. These proteins underscore RU's selective perturbation of proliferative and cytokine-driven signaling in AML, highlighting its ability to disrupt JAK/STAT and MAPK-mediated survival circuits. Cluster 4 is represented by CKAP5, emphasizes RU's capacity to target mitotic fidelity, microtubule organization, and centrosome-associated checkpoints critical for AML cell proliferation.

Clusters 8 and 9 include CCNA2, BLM, TP53BP1, and CUL4B, which converge on TP53-regulated transcription, cell-cycle checkpoints, DNA repair, and SUMOylation pathways. These hits highlight RU's ability to modulate both the replication stress response and apoptotic signaling, directly affecting AML cells' capacity to tolerate DNA damage and maintain checkpoint control.

Chromatin and epigenetic regulators are represented in Cluster 11 by EED and in Cluster 16 by HDAC2 and NPM1, reflecting enrichment in PRC2-mediated histone methylation, chromatin organization, transcriptional regulation by TP53, and SUMOylation. These perturbations suggest RU selectively interferes with transcriptional and epigenetic programs that sustain leukemic stemness and survival.

Cluster 22, represented by COPA, highlights vesicle transport and Golgi-to-ER trafficking pathways, indicating RU-mediated disruption of intracellular protein trafficking, a process increasingly recognized as critical for stress adaptation in AML. Finally, Cluster 32 includes CTSD, linked to extracellular matrix organization and collagen degradation, revealing RU's potential to modulate AML–niche interactions and extracellular remodeling.

Collectively, these RU-specific targets reveal a coordinated disruption of signaling cascades, cell-cycle regulation, DNA damage repair, chromatin and transcriptional control, and microenvironmental interactions. By converging on these vulnerabilities, RU achieves selective perturbation of AML networks that complement the effects of other combinatorial treatments, supporting its potential to overcome survival and compensatory signaling pathways in leukemic cells.

This combination-focused view highlights how RU uniquely undermines AML cell survival by derailing logistics, rewriting the epigenome, rewiring intercellular signaling, and collapsing mitotic fidelity.

PTM Enrichment analysis of differentially soluble proteins

We were also interested in investigating the post-translational modification (PTM) status of protein targets in order to assess their potential role in therapy response. To get an idea of what PTMs might be potentially present on target proteins in extract and intact samples, we utilized the PEIMAN2 R package[45]. Interestingly, significantly enriched PTM terms were different between extract and intact samples (Supplementary Figs. 2, 3). For example, phosphorylation of tyrosine, serine, and threonine, together with acetylation of lysine, showed significant enrichment in living cells. However, samples treated with drugs after the extraction of proteins showed significant enrichment in dimethylation of arginine and acetylation of lysine, methionine, and alanine. These observations imply that acetylation and methylation may be involved in direct binding of drugs, while phosphorylation and acetylation are signatures of the secondary cell response to the treatment.

To confirm the predictions of the PEIMAN2, we searched proposed PTMs in the proteomics data. Collectively, among 1280 protein targets after ruxolitinib, ulixertinib, and RU treatment in living cells, we found phosphorylation of tyrosine on 10 proteins (Fig. 10A). On the other hand, treatment with LS (either single drug or combination) in living cells yielded 950 proteins, among which 42 carried various PTMs (phosphorylation of serine and threonine, and acetylation of lysine) (Fig. 10B). In the case of extract samples, treatment with RU and LS showed 19 (975 in total) and 28 (626 in total) proteins with PTMs, respectively, comprising acetylation on alanine, methionine, and lysine, and dimethylation of arginine (Source Data File). Overall, this data shows that there is an involvement of PTMs in a cell response to the anti-AML treatment.

Next, we were interested in whether AML-related CoPISA protein targets (Fig. 10) are post-translationally modified. PTMs were detected on proteins across multiple clusters in both RU and LS treatments, with some overlap and distinct patterns between the two. Under RU treatment, DYNC1I1 (cytoplasmic dynein 1 intermediate chain 1) from C1 was acetylated on K42, a modification not previously reported. BLM (RecQ-like DNA helicase BLM) and NPM1 were also modified, with *BLM* showing dimethylation and both BLM and NPM1 displaying acetylation (Fig. 10C). In addition to acetylation and dimethylation, tyrosine phosphorylation was observed; for example, GSK3A/B in C4 was phosphorylated on Y279, and MCM2 in C6 on Y137. PPIA in C8 was also acetylated on K155. Under LS treatment, the highest number of modified protein targets was found in C3. ASH2L was phosphorylated simultaneously at T307, T310, and T311, while CBX3 showed phosphorylation at S95 and S176. H4C1 was acetylated at K9 and K13 on the same peptide. In contrast, C6 included only one modified protein, YWHAE, with N-acetylation on M1. In C7, CNOT3 was phosphorylated on S299.

Surprisingly, several AML-related CoPISA protein targets that were modified were exclusively targeted by combination treatment (*AND* gate). For example, BLM and NPM1 proteins are involved in the SUMOylation process as proteins that are SUMOylated and uniquely targeted by RU and not by any single drug. Notably, protein BLM included dimethylation (R483), which has not been reported before, and acetylation (K484) simultaneously on the same peptide. Additionally, on both proteins, lysines are sites for acetylation as well as SUMOylation (K484 in BLM and K267 in NPM1). Protein NPM1 is shown to be retained in the nucleoplasm when acetylated, while its nucleolar residency is prevented by SUMOylation[46,47]. It implies that different modifications on the same site can trigger different outcomes for the cell. BLM is a helicase that is involved in DNA replication and repair[48]. While acetylation regulates the function of BLM in response to DNA damage, SUMOylation is crucial for interaction with RAD51 protein in homologous recombination repair, localization to PML nuclear bodies, and BLM turnover[49,50]. Thus, different functions and the localization of the *BLM* protein can be triggered through the same modification site.

These findings highlight the complex interplay between identified PTMs and AML-related protein function, suggesting that specific modifications induced by RU and LS combination treatments may act as key regulatory switches controlling protein localization, interactions, and activity in leukemia cells.

Discussion

Combinatorial therapy has long been a cornerstone in oncology, particularly for aggressive malignancies like AML, due to its potential to overcome resistance and improve patient outcomes[51]. The classical rationale behind combinatorial regimens was to reduce the likelihood of resistance by employing multiple agents with distinct mechanisms of action, thus reducing the likelihood of clonal escape[52]. This principle has yielded durable responses in certain hematologic malignancies; however, in AML, the substantial genetic and epigenetic heterogeneity among patients continues to pose formidable challenges for identifying effective and broadly applicable combinations[53]. Moreover, the frequent emergence of therapy-resistant clones and the dose-limiting toxicities associated with multi-drug regimens have constrained their therapeutic window and limited their translational success[54]. These obstacles underscore the urgent need for strategies that rationally design and mechanistically dissect drug combinations to maximize efficacy while minimizing toxicity.

In this study, we introduced the CoPISA workflow to unravel the molecular underpinnings of combinatorial therapies in AML at a proteome-wide scale. These combinations were chosen based on prior computational and experimental work demonstrating that LS and RU provide the strongest balance of efficacy and low toxicity compared to first-line treatments. Specifically, a bipartite patient–drug network model identified them as top candidates, and follow-up studies confirmed their superior activity in AML lines and zebrafish xenografts, particularly in samples harboring high-risk mutations such as *TP53, MUC4, HLA-B*, and *FLT3*[9]. Unlike traditional methods that focus on additive or synergistic effects of individual agents, CoPISA captures drug-induced changes in protein solubility that specifically arise from the combined action of drugs, providing mechanistic insights into cellular responses unattainable by monotherapies. Applying CoPISA to two rationally designed AML drug pairs[8], LY3009120-sapanisertib (LS) and ruxolitinib-ulixertinib (RU), we observed that these combinations elicit combinatorial effects on protein stability, indicative of complex biological interactions rather than mere additive perturbations.

We propose that these unique solubility shifts likely arise from network-level phenomena, including cascades of protein-protein interactions, post-translational modifications (PTMs), and potential changes in subcellular localization triggered by combined pathway perturbations. To formalize this observation, we introduce the concept of *conjunctional targeting or inhibition*, describing proteins whose solubility is significantly altered only under combination treatment compared to single-drug conditions and control. This “AND-gate”-like behavior represents a conceptual advance over traditional models of synergy and aligns with emerging evidence that multi-agent therapies can reprogram cellular networks in fundamentally distinct ways. We view conjunctional targeting as a proof-of-principle approach that can evolve into a powerful tool for rational drug combination design, particularly when screening large candidate sets in a disease-specific context. By leveraging solubility-based responses, CoPISA offers a scalable strategy to prioritize synergistic drug pairs that reprogram cellular networks in fundamentally distinct ways.

Logic-based and Boolean modeling frameworks have previously been applied in AML to integrate causal signaling networks with patient-specific genomic information and to infer how co-occurring genetic perturbations propagate to hallmark phenotypes such as proliferation, differentiation, and apoptosis. For example, Palma et al. constructed AML-specific causal networks and derived Boolean models to predict phenotypic outputs arising from combinations of driver gene mutations[55]. These approaches operate primarily at the level of in silico phenotype inference based on prior network topology. In contrast, CoPISA provides an experimental, proteome-wide readout of how drug combinations reshape protein solubility and stability in lysate and intact-cell contexts, enabling direct identification of combination-exclusive “AND-gate” protein targets and emergent network rewiring. Thus, rather than predicting expected combinatorial behavior, CoPISA empirically captures molecular consequences of co-treatment. Importantly, the LS and RU combinations interrogated here were previously identified through patient-derived drug-response modeling and validated across AML cell lines, primary patient samples, and zebrafish xenograft models, and CoPISA mechanistically dissects these established combinatorial phenotypes[8,9].

Although demonstrated here using two rationally selected drug pairs in AML, the CoPISA framework is conceptually independent of specific compounds or disease context. CoPISA measures

https://doi.org/10.1038/s41467-026-70394-3

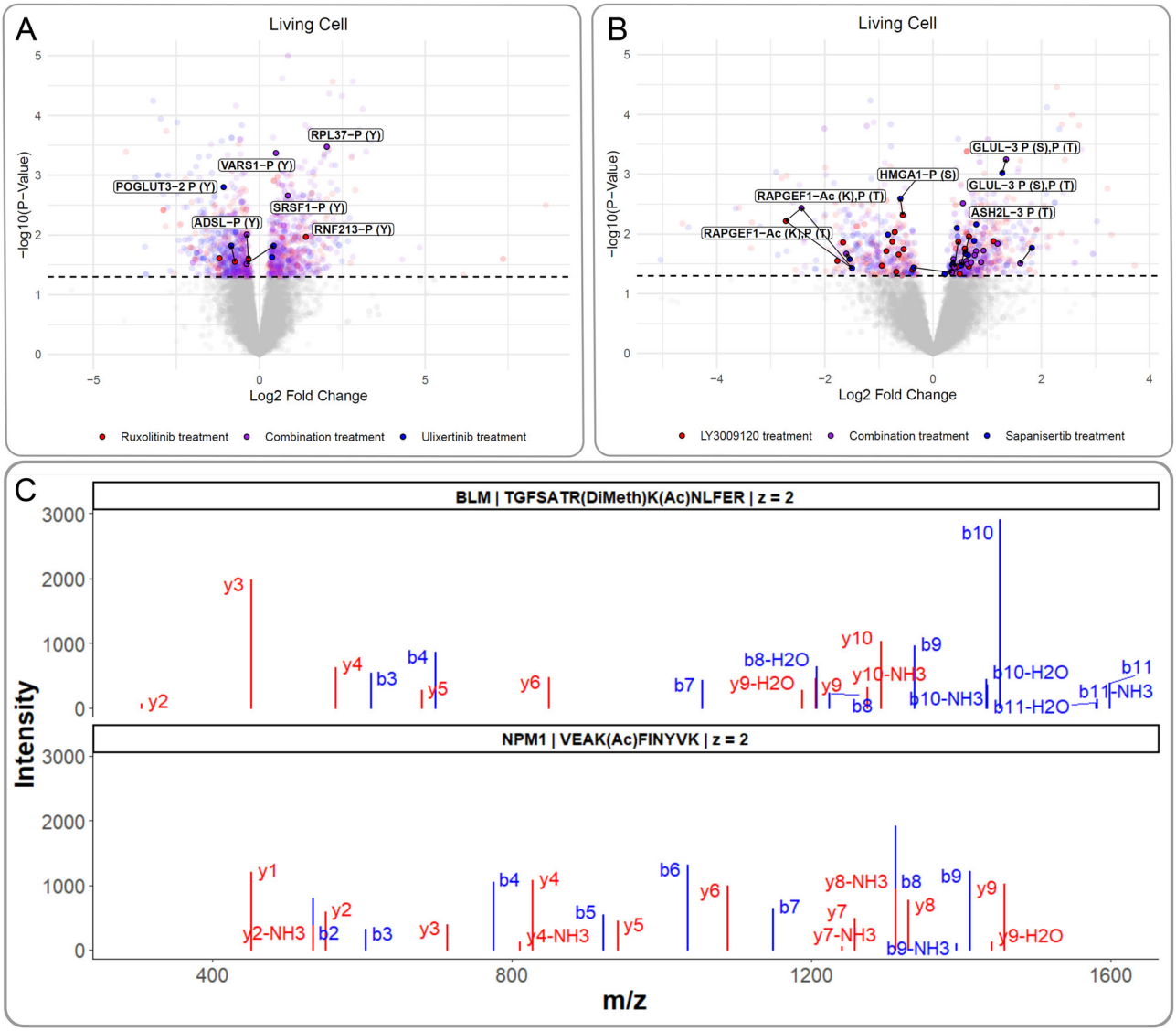

Fig. 10 | PTM status of CoPISA-identifi ed protein targets in living cells. A Cells were treated with ruxolitinib (3 μM;red), ulixertinib (3 μM; blue), or their combination (RU; purple). **B** Cells were treated with LY3009120 (red), sapanisertib (500 nM; blue), or their combination (LS; purple). Thevolcano plots are derived from Fig. 3, with proteins shown as semi-transparent points when no PTMs were detected in the mass spectrometry data and as opaque points when one or more PTMs were identified on their corresponding peptides. PTM names and modification sites are indicated after the protein identifier, separated by a hyphen (e.g., P61927-P(Y)). Multiple PTMs identified on the same peptide are listed separated by commas (e.g., Q13905-Ac(K), P(T)). Arrows indicate solubility changes of the same protein across different treatment conditions. Some labels were omitted to improve plot readability. Abbreviations: P(Y), tyrosine phosphorylation; P(T), threonine phosphorylation; P(S), serine phosphorylation; Ac(K), lysine acetylation. **C** Representative MS/MS spectra of modified peptides from BLM and NPM1 proteins. For clarity, only b-ions (blue) and y-ions (red) are shown. PTM annotation is overlaid onto proteins identified as significant in the corresponding analyses shown in Fig. 3; no additional statistical testing was provided in this figure. Source data are provided as a Source Data File.

perturbation-induced protein solubility/stability changes, a general physicochemical property that can be interrogated for diverse small-molecule combinations and other perturbation types. Likewise, the classification of solubility responses into single-agent, overlapping (OR-gate-like), and combination-exclusive (AND-gate-like) patterns arises from the experimental design rather than AML-specific biology. We therefore view conjunctional targeting as a generalizable descriptor of combination-specific stability alterations that may emerge whenever multiple perturbations cooperatively reshape protein states. The present study thus serves as a proof-of-principle for the broader applicability of CoPISA to mechanistic dissection of combinatorial therapies.

Differences in the number of proteins affected by combination treatment between lysate-based and living-cell CoPISA likely reflect the complexity of the cellular context. In lysates, solubility shifts primarily indicate direct compound-protein interactions, whereas intact cells capture secondary effects such as PTMs, PPIs, and signaling cascades. These emergent processes can amplify or attenuate solubility changes, leading to divergent patterns across experimental formats. The absence of a general trend is consistent with the context-dependent nature of PTM and PPI effects on protein stability[56].

Previous proteomic profiling in AML has revealed subtype-specific vulnerabilities. For example, Jayavelu et al. demonstrated proteogenomic subtypes defined by mitochondrial activity, ribosome biogenesis, and proteostasis, which predict therapy response[57]. Similarly, Tyner et al. identified signaling heterogeneity across AML samples using functional genomics, emphasizing MAPK and JAK/STAT pathways as potential combination targets[5]. While these

studies highlighted the diversity of AML dependencies, they did not interrogate emergent proteomic changes unique to drug combinations. Our CoPISA workflow advances the field by resolving combination-specific protein stability shifts, enabling mechanistic dissection of combinatorial drug effects at a proteome-wide scale. Furthermore, classical synergy screens, such as those employing Bliss[58] or Loewe[59] models, quantify functional synergy but offer limited mechanistic resolution. In contrast, CoPISA directly captures the conformational and stability changes of proteins in response to drug co-treatment, providing insights into network rewiring and actionable vulnerabilities. Notably, our finding that 47% of LS-perturbed and 54% of RU-perturbed AML-associated genes were unique to the combinations highlights the prevalence of conjunctional effects in AML cells.

The integration of *AND* and *OR* logic gates into our CoPISA analysis provides a powerful systems-level perspective on how LS and RU combinations reprogram leukemic cell function to achieve synergistic effects. The enrichment of SUMOylation, chromatin condensation, and mitotic control pathways in the LS *AND* gate highlights the ability of this combination to destabilize genome integrity and impair cell division fidelity, two hallmarks of AML proliferation and resistance[60]. Simultaneously, disruption of RNA processing and immune-related pathways in intact cells suggests that LS not only targets intrinsic leukemic signaling but also modulates the tumor microenvironment to potentially enhance immune clearance[61]. The complementary effects of RU, which prominently engages transcriptional regulation, epigenetic modulation, and apoptosis pathways under the *AND* gate, underscore its capacity to restore tumor suppressor networks and induce metabolic collapse in AML cells[62,63]. Notably, the convergence of LS and RU effects on phospholipid metabolism and RNA splicing across both gating models and cellular fractions suggests that these core biosynthetic processes represent shared vulnerabilities in AML. Together, these findings provide a mechanistic rationale for how conjunctional targeting in LS and RU treatments exerts multi-axis pressure on AML survival networks, overwhelming adaptive resistance and supporting the development of rational, precision-guided combinatorial regimens.

The functional network analysis of AML-associated genes and PTM enrichment analysis provide critical mechanistic insight into how the LS and RU combinations reprogram leukemia-specific signaling and survival pathways to achieve therapeutic synergy. LS treatment prominently engaged modules involved in epigenetic regulation (DNMT3A, ASH2L, RBBP7) and PTEN transcriptional control, suggesting a capacity to disrupt the chromatin architecture of AML and restore tumor-suppressive pathways such as PI3K-AKT inhibition[64,65]. In contrast, RU targeted an overlapping yet distinct set of vulnerabilities, including NPM1 and TP53, two of the most frequently mutated and therapeutically challenging nodes in AML. *NPM1* mutations, which occur in approximately 30% of AML cases, promote aberrant cytoplasmic localization and impair genomic stability and ribosomal biogenesis[66]. TP53 mutations, present in ~10% of AML and associated with chemoresistance and poor prognosis, disrupt DNA damage checkpoints and apoptosis[67]. The engagement of RU with SUMOylation networks and cohesion/spindle assembly proteins (e.g., *SMC1A*, *CKAP5*), indicating a potential to induce mitotic catastrophe and disrupt genomic surveillance mechanisms essential for leukemic persistence[68]. Shared perturbations in MAPK/ERK and PI3K/AKT signaling across both combinations highlight these pathways as central hubs of AML pathogenesis and promising points for combinatorial intervention[69]. Collectively, these findings reinforce that LS and RU act not merely through additive inhibition but by simultaneously destabilizing multiple survival axes, including epigenetic, metabolic, and immune regulatory networks, to overwhelm AML cells' adaptive capacity. This network-centric perspective also highlights potential biomarkers and actionable targets (e.g., DNMT3A, NPM1, PTEN) that could inform precision therapy approaches for genetically diverse AML subtypes.

Finally, prospective clinical evaluation of LS and RU regimens, guided by biomarkers like *DNM3A, NPM1, and TP53* status, could advance precision medicine approaches for genetically diverse AML subtypes.

Methods

Ab Initio simulation

The simulation of sigmoidal curves of 10000 hypothetical proteins was carried out using R, and melting temperatures T_m, selected randomly in the range from 48 to 56 °C. $N_t = 15$ temperature points between 45 and 59 °C with a 1 °C step were chosen. Sigmoidal melting curves were simulated by calculating the relative intensity $I(T)$ for a given temperature T as $Intensity(T)_{control} = 0.5 \times erf[(T_m - T)/sqrt(T_m)/2$ where erf is the error function and sqrt is the square root function. Similarly, sigmoidal melting curves for treated samples was simulated as $Intensity(T)_{treated} = 0.5 \times erf[(T_m + \Delta T_m - T)/sqrt(T_m + \Delta T_m)/2$. $\triangle T_m$ were simulated as random values in the range between -3°C and +3°C. The sum of measured signals for control and treated samples is calculated as $S_m = \sum_{T=1}^{15} Intensity(T)$, for all temperature points. The treatment here was simulated for two hypothetical drugs to calculate S_m values, i.e., $S_m^{control}$, S_m^1 and S_m^2. In the next step, we calculated the two $\triangle S_m$ for both hypothetical drugs, i.e., $\triangle S_m^1$ and $\triangle S_m^2$ in 10,000 proteins to depict versus each other.

Cell culture

MOLM-13, MOLM-16, SKM, and NOMO-1 cells were obtained from Deutsche Sammlung von Mikroorganismen und Zellkulturen (DSMZ, Germany) and cultured in RPMI-1640 medium (Gibco, Thermo Fisher Scientific, USA) supplemented with 10–20% fetal bovine serum (FBS) (Gibco, Thermo Fisher Scientific), 2 mM L-glutamine (Lonza), and 100 units/mL penicillin/streptomycin (Gibco, Thermo Fisher Scientific) at 37 °C and 5% CO_2. Cells were harvested and centrifuged at 400 × *g* for 4 min. All cell lines were tested for mycoplasma contamination using PCR-based assays to confirm the absence of infection. The cell lines were checked against the International Cell Line Authentication Committee (ICLAC) database of cross-contaminated or misidentified cell lines, and none were listed.

Cell lysate-based CoPISA

For each treatment condition, three technical replicates were performed per cell line, and experiments were conducted across four biological replicates corresponding to four different AML cell lines (MOLM-13, MOLM-16, SKM, and NOMO-1). Cells were cultured until they reached the desired density of 2×10^6 cells per treatment with seven different treatment groups for each cell line, performed in triplicate. A 24 ml volume of cell culture was pelleted by centrifugation at 600 × *g* for 5 min, followed by two washes with phosphate-buffered saline (PBS). After a final pelleting, cells were resuspended in PBS (GIBCO) supplemented with protease inhibitors (Roche, Switzerland). The cell mixture was lysed through 4 cycles of freezing in liquid N_2 and then thawing at 35 °C. At the final step, cells were cleared by centrifugation at 10,000 × *g* for 10 min at 4 °C.

Samples were then treated with single or combination drug regimens at the following concentrations: LY3009120 500 nM, sapanisertib 500 nM, ruxolitinib 3 µM, and ulixertinib 3 µM for 15 min at room temperature. For the treatment of control samples, 0.1% DMSO was used. After treatment, the samples were aliquoted into 12 equal volumes for subsequent heat treatments. Each aliquot was subjected to a 3-minute heat treatment at temperatures ranging from 48 °C to 59 °C in 1 °C intervals using a thermocycler (Applied Biosystems Veriti).

After equilibrating at room temperature for 3 min, samples from different temperatures for each drug treatment were pooled and subjected to ultracentrifugation at 100,000 g for 20 min at 4 °C (Beckman Colter Optima Max-XP). The soluble proteins from the supernatant were collected for further analysis.

Living cell-based CoPISA

Living-cell CoPISA experiments were likewise performed with three technical replicates per treatment per cell line, across four biological replicates (four AML cell lines: MOLM-13, MOLM-16, SKM, and NOMO-1). Cells (2×10^6 cells per condition) were treated with a single or combination drug with concentrations mentioned in 6-well plates and incubated at 37 °C with 5% CO_2 for 60 min. Following treatment, the cells were washed twice with PBS and resuspended in 320 μL of PBS supplemented with a protease inhibitor. An equal volume of each sample was transferred to the PCR plate and was heated for 3 min at the same temperatures used in the lysate-based protocol. The samples were allowed to cool down at room temperature for 3 min and then applied for four cycles of freezing cells in liquid N_2 and thawing at 35 °C. After pooling the samples from different temperature points for each treatment, the soluble proteins were isolated via ultracentrifugation at 100,000 × *g* for 20 min at 4 °C. At this point, samples were flash frozen and stored at − 80 °C for future analysis.

Experimental design

Quantitative proteomics was performed using tandem mass tag (TMT)–based multiplexed LC–MS/MS. Across the entire study, a total of 16 independent TMT16-plex experiments were acquired, corresponding to multiple biological samples derived from four human leukemia cell lines (SKM, MOLM13, MOLM16, and NOMO) analyzed under different treatment conditions and sample preparation modes (INTACT vs EXTRACT). Each TMT set contained up to 13 biological samples, representing distinct treatment conditions (including untreated control, single-drug, and combination treatments), as well as one pooled reference channel generated by mixing equal peptide amounts from all samples within the same TMT set. Each treatment condition was analyzed in three technical replicates ($n = 3$) per TMT set, and biological replication was provided by the use of four independent cell lines ($n = 4$).

Proteomics sample processing

Protein concentration was measured using the Pierce BCA Protein Assay Kit (Thermo), and the volume corresponding to 27 μg of protein was transferred from each sample to prepared filter tubes (Amicon Ultra-0.5 mL Centrifugal Filters 10KD). The volume of each sample was adjusted to an equal level using 20 mM 4-(2-hydroxyethyl)-1-piperazinepropanesulfonic acid (EPPS) buffer, then was reduced in 10 mM dithiothreitol (55 °C, 30 min) and alkylated in 50 mM iodoacetamide (25 °C, 60 min in darkness).

After reduction and alkylation, samples were centrifuged for 20 min at 14000 g, followed by two washes. The EPPS buffer was then added to the Amicon filter tubes containing samples. Proteins were digested overnight at 37 °C with vigorous shaking by trypsin at a ratio of 1:50. The resulting peptides were collected by centrifugation and rinsing the filter tubes with EPPS. Prior to labeling, equal peptide amounts from each treatment group were mixed to generate pooled reference samples. For TMT labeling, 25 μg of peptides per sample were labeled using tandem mass tag (TMT) reagents according to the manufacturer's protocol (Thermo Fisher Scientific). For each TMT experiment, three technical replicates per treatment condition (drug A, drug B, drug combination AB, and untreated control), together with one pooled reference channel, were combined. This resulted in a final multiplexed mixture of 325 μg total peptide per TMT set (13 labeled channels × 25 μg per channel).

Peptide fractionation and LC MS/MS analysis

TMT-labeled peptides were fractionated and analyzed by high-pH reversed-phase chromatography using an Ultimate 3000 system (Thermo Fisher Scientific). Peptides were separated using a gradient from 2% to 15% buffer B over 3 min, to 45% B over 59 min, to 80% B over 3 min, followed by a 9 min hold at 80% B, re-equilibration to 2% B over 1 min, and a 15 min hold at 2% B[70]. Fractions were concatenated to yield 12 final fractions per TMT set, which were analyzed independently by LC–MS/MS.

LC–MS/MS analysis was performed on an Orbitrap Eclipse Tribrid mass spectrometer equipped with an Ultimate 3000 nanoLC system and FAIMS Pro interface (Thermo Fisher Scientific). Peptides were separated on an in-house packed C18 analytical column operated at nanoflow rates. Data were acquired in data-dependent acquisition mode using SPS-MS3 for TMT quantification. MS1 spectra were acquired in the Orbitrap, MS2 spectra were acquired in the ion trap, and MS3 spectra were acquired in the Orbitrap. FAIMS compensation voltages of − 40 V and − 70 V were alternated during acquisition. Dynamic exclusion was enabled. Real-time search (RTS) was performed using a human database containing 20362 entries downloaded from Uniprot on 20200417.

Database search and protein identification

Raw files were processed using MaxQuant version 2.6.5.0, incorporating the Andromeda search engine. Spectra were searched against a reviewed human UniProt protein sequence database (Swiss-Prot) downloaded on 20241010, with a reversed decoy strategy and common contaminants included. Group-specific parameters were used as follows. The type of the search was set to Reporter MS3. Isobaric labels and their correction factors were provided according to the manufacturer kit sheet. Normalization was set to a weighted ratio to the reference channel. Variable modifications were set to oxidation of methionines and acetylation of N-termini, while fixed modification settings contained only carbamidomethylation of cysteines. The maximum number of modifications per peptide was set to 3. Two missed cleavages with Trypsin/P were allowed. For the refined search, all settings were kept as in the original with the addition of variable modifications as proposed by the PEIMAN2 R package, with five as a maximum number of modifications per peptide.

Precursor mass tolerances were set to 20 ppm for the first search, and 4.5 ppm for the main search, with internal mass recalibration enabled. Peptides of at least 7 amino acids and precursor charge states up to 7 were considered. TMT reporter ion intensities were quantified in Reporter MS3 mode using manufacturer-provided isotope impurity correction factors, and channel intensities were normalized by a weighted ratio to the pooled reference channel. PSM-, peptide-, protein-, and site-level FDRs were controlled at 1% using the target–decoy strategy. Protein identifications required at least one razor or unique peptide.

LC-MS Analysis of drug combinations

Ten picomoles from each drug, separately or combined, were injected into LCMS (Eksigent Ekspert 400 coupled to TripleTOF 6600 (Sciex, USA)). These analytes were separated using a linear gradient of 15 min comprising 8 min from 3% to 35% of solution B (0.1% formic acid/acetonitrile) and 2 min to 90% of solution B on a reverse phase C4 column (0.3 × 20 mm, Phenomenex, USA). The solution A was 0.1% formic acid, and the flow rate was at 5 μl/min. The mass spectrometer was set in TOF MS mode with the following parameters: Ion spray voltage was at 5500 volts, and ion source and curtain gases were 10 and 30 liters per minute, respectively. TOF MS was acquired from m/z 200 to 1500. Following LC-MS acquisition, raw files were analyzed by PeakView® software, version 2.2 (Sciex). Drug ions were extracted using their corresponding m/z +/− 0.5 Da.

PTM Enrichment analysis

PTM enrichment analysis was performed utilizing the PEIMAN2 R package. Firstly, a ranked list (by *p*-value of statistical test from the limma package) of differentially soluble proteins with their UniProt Accession numbers was created for every treatment condition. Next, the function runPSEA() was executed to perform protein set enrichment analysis. Results were filtered based on the number of proteins enriched for every PTM term (≥10) and the significance of the enrichment (0.05). These PTMs were provided as modification values as input to perform the refined search by MaxQuant proteomics software.

Statistical analysis

Proteomics data were obtained from primary Peptide Spectrum Match (PSM) reports, providing raw intensity values of peptides identified across experimental conditions. Reverse hits and potential contaminants were removed, and proteins lacking quantification across the selected samples were excluded prior to modeling. Protein-level intensity matrices were extracted per condition and analyzed on a log2 scale using log2(x + 1) transformation to stabilize variance across the dynamic range. A pooled control sample was used for further normalization, and protein intensities were averaged across replicates to create matrices for each treatment condition.

Differential solubility effects were estimated using linear modeling with empirical Bayes moderation (limma). For each condition-specific matrix, a design matrix without intercept was constructed using treatment groups as factors, and predefined contrasts were tested comparing Control (C) against each single agent and the combination (i.e., C−R, C−U, C−RU; or C−L, C−S, C−LS). Moderated t-statistics were used to obtain P-values. For each contrast, volcano plots display log2 fold-change (x-axis; estimated from the fitted contrast) versus −log10(P-value) (y-axis), highlighting proteins meeting the nominal significance criterion (*P*-value < 0.05). We generated superimposed volcano plots to provide an overview across related contrasts within the same condition; proteins recurring as significant in more than one comparison are emphasized by a black outlined circle marker to facilitate identification of consistently perturbed proteins. Fold change plots comparing each combination of treatments (comb vs. drug 1 and comb vs. drug 2) were generated to assess concordance and divergence between single-agent and combination effects, with primary plots displaying fold changes across the full dataset range and inset plots highlighting a focused subset of the most significant proteins based on *p*-values. We reported both statistical significance and effect size, and use the fold-change threshold primarily as an interpretability guide rather than as the sole criterion for candidate selection. Due to the complexity of comparing single drugs and combinations in the CoPISA method and the lack of an a priori error model in a low-power proteomics context[71], direct multiple hypothesis correction was not feasible. To address this, we tested our candidate selection procedure and estimated the false discovery rate (FDR) for proteins with significant solubility shifts. This involved permuting the protein S_m values across replicates within the dataset to generate 1000 randomized permutations[72–74]. The same selection criteria were applied to these permuted datasets as to the original data, enabling us to evaluate the robustness of our approach and ensure confidence in the identified candidates.

AML-Related network construction and functional annotation workflow

The signaling network dataset was obtained from Reactome and preprocessed by removing duplicate edges. Subsequently, AML-associated gene mutations were downloaded from two sources: DEPMAP (for cell lines) and the FIMM-AML cohort (for patient data). Mutations were filtered using a stringent threshold (*p*-value < $10e^{-8}$), and only those classified as high-impact, such as frameshift mutations, nonsense mutations (introducing stop codons), and similar functionally disruptive variants, were retained. A directed network was then reconstructed by first filtering the global Reactome network to retain only the curated AML-mutated genes and known AML-related drug targets. This step ensured that only AML-associated nodes were included. For every pair of these AML-associated nodes, we computed the directed shortest path. All intermediate nodes appearing in any of these shortest paths were then used to induce a subnetwork from the original Reactome signaling network. The resulting edge list was extracted to form the final AML-specific signaling network. Network topology analysis was performed, and downstream analyses focused on the largest connected component, which comprised 658 nodes. Community detection was carried out using multiple algorithms, including Louvain, Walktrap, and Infomap. Among these, the Infomap algorithm was selected for further analysis due to its superior modularity score. Following community detection, functional annotation was performed to identify biological pathways enriched in each cluster and treatment group. Proteins were grouped by treatment and cluster and mapped to Entrez IDs. Reactome pathway enrichment analysis was then carried out using ReactomePA with adjusted thresholds (p-value < 0.05). Reactome pathway enrichment was performed using ReactomePA with Benjamini–Hochberg correction for multiple testing. This analysis highlighted key signaling pathways associated with AML-specific communities and drug responses within the reconstructed network.

Reporting summary

Further information on research design is available in the Nature Portfolio Reporting Summary linked to this article.

Data availability

The mass spectrometry proteomics data generated in this study have been deposited in the ProteomeXchange Consortium[75] via the PRIDE partner repository[76,77] under accession code PXD066812. There are no restrictions on data availability. Source data are provided in this paper.

Code availability

The analysis code used in this study is publicly available at https://github.com/jafarilab/CoPISA_RULS (https://doi.org/10.5281/zenodo.18669347).

References

1. Döhner, K., Paschka, P. & Döhner, H. [Acute myeloid leukemia]. *Internist* **56**, 354–363 (2015).
2. Cherry, E. M. et al. Venetoclax and azacitidine compared with induction chemotherapy for newly diagnosed patients with acute myeloid leukemia. *Blood Adv.* **5**, 5565–5573 (2021).
3. Karol, S. E. et al. Venetoclax in combination with cytarabine with or without idarubicin in children with relapsed or refractory acute myeloid leukaemia: a phase 1, dose-escalation study. *Lancet Oncol.* **21**, 551–560 (2020).
4. Mason-Osann, E., Pomeroy, A. E., Palmer, A. C. & Mettetal, J. T. Synergistic Drug Combinations Promote the Development of Resistance in Acute Myeloid Leukemia. *Blood Cancer Discov.* **5**, 95–105 (2024).
5. Tyner, J. et al. Functional genomic landscape of acute myeloid leukemia. *Nature* **562**, 526–531 (2018).
6. Tang, K., Schuh, A. C. & Yee, K. W. 3+7 Combined chemotherapy for acute myeloid leukemia:is it time to say goodbye? *Curr. Oncol. Rep.* **23**, 120 (2021).
7. Wang, J., Tomlinson, B. & Lazarus, H. M. Update on small molecule targeted therapies for acute myeloid leukemia. *Curr. Treat. Options Oncol.* **24**, 770–801 (2023).

8. Mirzaie, M. et al. Designing patient-oriented combination therapies for acute myeloid leukemia based on efficacy/toxicity integration and bipartite network modeling. *Oncogenesis* **13**, 11 (2024).
9. Gholizadeh, E. et al. Targeting acute myeloid leukemia resistance with two novel combinations demonstrate superior efficacy in TP53, HLA-B, MUC4 and FLT3 mutations. *Biomed. Pharmacother.* **192**, 118647 (2025).
10. Mateus, A., Määttä, T. A. & Savitski, M. M. Thermal proteome profiling: unbiased assessment of protein state through heat-induced stability changes. *Proteome Sci.* **15**, 13 (2016).
11. Zangene, E. et al. DORSSAA: Drug-target interactOmics resource based on stability/solubility alteration assay. Preprint at https://doi.org/10.1101/2023.12.29.573639 (2023).
12. Gaetani, M. et al. Proteome integral solubility alteration: a high-throughput proteomics assay for target deconvolution. *J. Proteome Res.* **18**, 4027–4037 (2019).
13. Saei, A. A. et al. Multifaceted proteome analysis at solubility, redox, and expression dimensions for target identification. *Adv. Sci.* **11**, e2401502 (2024).
14. Van Vranken, J. G. et al. Large-scale characterization of drug mechanism of action using proteome-wide thermal shift assays. *eLife* **13**, RP95595 (2024).
15. Franken, H. et al. Thermal proteome profiling for unbiased identification of direct and indirect drug targets using multiplexed quantitative mass spectrometry. *Nat. Protoc.* **10**, 1567–1593 (2015).
16. Savitski, M. M. et al. Tracking cancer drugs in living cells by thermal profiling of the proteome. *Science* **346**, 1255784 (2014).
17. Jafari, M., Ansari-Pour, N., Azimzadeh, S. & Mirzaie, M. A logic-based dynamic modeling approach to explicate the evolution of the central dogma of molecular biology. *PLoS ONE* **12**, e0189922 (2017).
18. Tajan, M., de Rocca Serra, A., Valet, P., Edouard, T. & Yart, A. SHP2 sails from physiology to pathology. *Eur. J. Med. Genet.* **58**, 509–525 (2015).
19. Chen, Y., Ouyang, Y., Li, Z., Wang, X. & Ma, J. S100A8 and S100A9 in cancer. *Biochim. Biophys. Acta Rev. Cancer* **1878**, 188891 (2023).
20. Tian, C. et al. UCHL1 promotes cancer stemness in triple-negative breast cancer. *Pathol. Res. Pract.* **240**, 154235 (2022).
21. Meng, Y. et al. Research advances in the role of the tropomyosin family in cancer. *Int. J. Mol. Sci.* **24**, 13295 (2023).
22. Estecha, A., Aguilera-Montilla, N., Sánchez-Mateos, P. & Puig-Kröger, A. RUNX3 regulates intercellular adhesion molecule 3 (ICAM–3) expression during macrophage differentiation and monocyte extravasation. *PLoS ONE* **7**, e33313 (2012).
23. Greuber, E. K., Smith-Pearson, P., Wang, J. & Pendergast, A. M. Role of ABL family kinases in cancer: from leukaemia to solid tumours. *Nat. Rev. Cancer* **13**, 559–571 (2013).
24. Carter, J. L. et al. Targeting multiple signaling pathways: the new approach to acute myeloid leukemia therapy. *Signal Transduct. Target. Ther.* **5**, 288 (2020).
25. Bottani, E. et al. TTC19 plays a husbandry role on UQCRFS1 turnover in the biogenesis of mitochondrial respiratory complex III. *Mol. Cell* **67**, 96–105 (2017).
26. Borkar, R. M. et al. An evaluation of the CYP2D6 and CYP3A4 inhibition potential of metoprolol metabolites and their contribution to drug-drug and drug-herb interaction by LC-ESI/MS/MS. *Biomed. Chromatogr.* **30**, 1556–1572 (2016).
27. Müller, S., Ledl, A. & Schmidt, D. SUMO: a regulator of gene expression and genome integrity. *Oncogene* **23**, 1998–2008 (2004).
28. Ghelli Luserna di Rorà, A., Martinelli, G. & Simonetti, G. The balance between mitotic death and mitotic slippage in acute leukemia: a new therapeutic window? *J. Hematol. Oncol.* **12**, 123 (2019).
29. Cheng, Y. et al. Tumor microenvironmental competitive endogenous RNA network and immune cells act as robust prognostic predictor of acute myeloid leukemia. *Front. Oncol.* **11**, 584884 (2021).
30. Trombetti, S. et al. Oxidative stress and ROS-mediated signaling in leukemia: Novel promising perspectives to eradicate chemoresistant cells in myeloid leukemia. *Int. J. Mol. Sci.* **22**, 2470 (2021).
31. Addanki, S., Kim, L. E. & Stevens, A. M. Understanding and targeting metabolic vulnerabilities in acute myeloid leukemia: An updated comprehensive review. *Cancers***17**, (2025).
32. Saraon, P. et al. Receptor tyrosine kinases and cancer: oncogenic mechanisms and therapeutic approaches. *Oncogene* **40**, 4079–4093 (2021).
33. Tettamanti, S., Pievani, A., Biondi, A., Dotti, G. & Serafini, M. Catch me if you can: how AML and its niche escape immunotherapy. *Leukemia* **36**, 13–22 (2021).
34. Pabst, T. & Mueller, B. Transcriptional dysregulation during myeloid transformation in AML. *Oncogene* **26**, 6829–6837 (2007).
35. Biffo, S., Ruggero, D. & Santoro, M. M. The crosstalk between metabolism and translation. *Cell Metab.* **36**, 1945–1962 (2024).
36. Crews, L. A. et al. RNA splicing modulation selectively impairs leukemia stem cell maintenance in secondary human AML. *Cell Stem Cell* **19**, 599–612 (2016).
37. Chen, C. & Zhang, J. Enhancing leukemia treatment: The role of combined therapies based on amino acid starvation. *Cancers* **16**, 1171 (2024).
38. Arafeh, R., Shibue, T., Dempster, J. M., Hahn, W. C. & Vazquez, F. The present and future of the Cancer Dependency Map. *Nat. Rev. Cancer* **25**, 59–73 (2025).
39. Malani, D. et al. Implementing a functional precision medicine tumor board for acute myeloid leukemia. *Cancer Discov.* **12**, 388–401 (2022).
40. Ciciarello, M., Corradi, G., Forte, D., Cavo, M. & Curti, A. Emerging bone marrow microenvironment-driven mechanisms of drug resistance in acute myeloid leukemia: Tangle or chance? *Cancers* **13**, 5319 (2021).
41. Teague, R. M. & Kline, J. Immune evasion in acute myeloid leukemia: current concepts and future directions. *J. Immunother. Cancer* **1**, 13 (2013).
42. Fan, C., Yang, X., Yan, L. & Shi, Z. Oxidative stress is two-sided in the treatment of acute myeloid leukemia. *Cancer Med.* **13**, e6806 (2024).
43. Yates, L. A., Zhang, X. & Burgers, P. M. DNA damage and replication stress checkpoints. *Annu. Rev. Biochem.* **94**, 195–221 (2025).
44. Weisberg, E. et al. Evaluation of ERK as a therapeutic target in acute myelogenous leukemia. *Leukemia* **34**, 625–629 (2020).
45. Nickchi, P. et al. Monitoring functional posttranslational modifications using a data-driven proteome informatic pipeline. *Proteomics* **25**, e202400238 (2025).
46. Liu, X. et al. Sumoylation of nucleophosmin/B23 regulates its subcellular localization, mediating cell proliferation and survival. *Proc. Natl. Acad. Sci. USA* **104**, 9679–9684 (2007).
47. Shandilya, J. et al. Acetylated NPM1 localizes in the nucleoplasm and regulates transcriptional activation of genes implicated in oral cancer manifestation. *Mol. Cell. Biol.* **29**, 5115–5127 (2009).
48. Langland, G. et al. The BLM helicase is necessary for normal DNA double-strand break repair. *Cancer Res.* **62**, 2766–2770 (2002).
49. Wang, Y. & Luo, J. Acetylation of BLM protein regulates its function in response to DNA damage. *RSC Adv.* **7**, 55301–55308 (2017).
50. Ouyang, K. J., Yagle, M. K., Matunis, M. J. & Ellis, N. A. BLM SUMOylation regulates ssDNA accumulation at stalled replication forks. *Front. Genet.* **4**, 167 (2013).
51. Pomeroy, A. E., Schmidt, E. V., Sorger, P. K. & Palmer, A. C. Drug independence and the curability of cancer by combination chemotherapy. *Trends Cancer Res.* **8**, 915–929 (2022).

52. He, L. et al. Methods for high-throughput drug combination screening and synergy scoring. *Methods Mol. Biol.* **1711**, 351–398 (2018).
53. Arnone, M. et al. Acute myeloid leukemia stem cells: The challenges of phenotypic heterogeneity. *Cancers* **12**, 3742 (2020).
54. Filì, C. et al. Efficacy and toxicity of Decitabine in patients with acute myeloid leukemia (AML): A multicenter real-world experience. *Leuk. Res.* **76**, 33–38 (2019).
55. Palma, A. et al. Integrating patient-specific information into logic models of complex diseases: Application to acute myeloid leukemia. *J. Pers. Med.* **11**, 117 (2021).
56. Price, J. L. et al. Context-dependent effects of asparagine glycosylation on Pin WW folding kinetics and thermodynamics. *J. Am. Chem. Soc.* **132**, 15359–15367 (2010).
57. Jayavelu, A. K. et al. The proteogenomic subtypes of acute myeloid leukemia. *Cancer Cell* **40**, 301–317 (2022).
58. Bliss, C. I. The toxicity of poisons applied jointly1. *Ann. Appl. Biol.* **26**, 585–615 (1939).
59. Loewe S. The problem of synergism and antagonism of combined drugs. *Arzneimittelforschung.* **3**, 285–290 (1953).
60. de Oliveira Lisboa, M., Brofman, P., Schmid-Braz, A. T., Rangel-Pozzo, A. & Mai, S. Chromosomal instability in acute myeloid leukemia. *Cancers* **13**, 2655 (2021).
61. Guan, L. et al. Regulation of the tumor immune microenvironment by cancer-derived circular RNAs. *Cell Death Dis.* **14**, 132 (2023).
62. Chen, Y., Chen, J., Zou, Z., Xu, L. & Li, J. Crosstalk between autophagy and metabolism: implications for cell survival in acute myeloid leukemia. *Cell Death Discov.* **10**, 46 (2024).
63. Wallwitz, J., Aigner, P. & Stoiber, D. Tumor suppressors in acute myeloid leukemia. *Leuk. Lymphoma* **62**, 2320–2330 (2021).
64. Ley, T. J. et al. DNMT3A mutations in acute myeloid leukemia. *N. Engl. J. Med.* **363**, 2424–2433 (2010).
65. Woods, B. A. & Levine, R. L. The role of mutations in epigenetic regulators in myeloid malignancies. *Immunol. Rev.* **263**, 22–35 (2015).
66. Falini, B., Sportoletti, P. & Martelli, M. P. Acute myeloid leukemia with mutated NPM1: diagnosis, prognosis and therapeutic perspectives. *Curr. Opin. Oncol.* **21**, 573–581 (2009).
67. Barbosa, K., Li, S., Adams, P. D. & Deshpande, A. J. The role of TP53 in acute myeloid leukemia: Challenges and opportunities. *Genes Chromosomes Cancer* **58**, 875–888 (2019).
68. Cuartero, S., Innes, A. J. & Merkenschlager, M. Towards a better understanding of cohesin mutations in AML. *Front. Oncol.* **9**, 867 (2019).
69. Steelman, L. S. et al. Roles of the Ras/Raf/MEK/ERK pathway in leukemia therapy. *Leukemia* **25**, 1080–1094 (2011).
70. Leuchtmann, A. B., Afifi, Y., Ritz, D. & Handschin, C. Effects of high-resistance wheel running on hallmarks of endurance and resistance training adaptations in mice. *Physiol. Rep.* **11**, e15701 (2023).
71. Pascovici, D., Handler, D. C. L., Wu, J. X. & Haynes, P. A. Multiple testing corrections in quantitative proteomics: A useful but blunt tool. *Proteomics* **16**, 2448–2453 (2016).
72. Saei, A. A. et al. Mapping the GALNT1 substrate landscape with versatile proteomics tools. https://doi.org/10.1101/2022.08.24.505189. (2022)
73. Saei, A. A. et al. System-wide identification and prioritization of enzyme substrates by thermal analysis. *Nat. Commun.* **12**, 1296 (2021).
74. Sabatier, P. et al. An integrative proteomics method identifies a regulator of translation during stem cell maintenance and differentiation. *Nat. Commun.* **12**, 6558 (2021).
75. Deutsch, E. W. et al. The ProteomeXchange consortium at 10 years: 2023 update. *Nucleic Acids Res.* **51**, D1539–D1548 (2023).
76. Perez-Riverol, Y. et al. The PRIDE database at 20 years: 2025 update. *Nucleic Acids Res.* **53**, D543–D553 (2025).
77. Perez-Riverol, Y. et al. PRIDE Inspector toolsuite: moving toward a universal visualization tool for proteomics data standard formats and quality assessment of poteomeXchange datasets. *Mol. Cell Proteom.* **15**, 305–317 (2016).

Acknowledgements

The authors acknowledge the Meilahti Clinical Proteomics Core Facility for Mass Spec. sample analysis (supported by HiLIFE and Biocenter Finland). We also thank Krister Wennerberg for helpful discussions and feedback on the manuscript. This study was financially supported by the Tampere Institute for Advanced Study, the Research Council of Finland [Grant 332454 to M.J.] and the Jane and Aatos Erkko Foundation [Grant 220031 to M.J.]. EZ's salary is partially supported by the iCANPOD postdoctoral program, which is funded through the iCANDOC doctoral education pilot in precision cancer medicine. A.A.S. acknowledges funding from the Swedish Cancer Society (24 3595 Pj), the Swedish Research Council (2023-02692), Åke Wibergs Stiftelse (M23-0186) and Jeanssons Stiftelse (J2023-0094). C.A.H is supported by funding from the Sigrid Jusélius Foundation, Cancer Foundation Finland (grant 4709178), Research Council of Finland (grants 357686, 352265, and 1320185), and the NIH (1R01 CA270210-01A1).

Author contributions

M.J. conceived the study and designed the research questions. M.J. and A.A.S. provided scientific direction, supervised the project, and contributed to the manuscript preparation. E.G. led the experimental analyses and data interpretation, while E.Z. led the computational analyses and data visualization. U.V. participated in proteomics data analysis, and D.R. conducted the proteomics mass spectrometry experiments and data analysis. J.J.M. assisted with protein extraction and interpretation of signaling networks. R.S. and M.B. contributed to small-molecule mass spectrometry analysis. M.W. supported the interpretation of findings and the validation of the experimental design. C.A.H. provided cell lines and contributed to the interpretation of findings. E.K. and P.A.H. offered valuable inputs on data interpretation and visualization.

Competing interests

C.A.H has received research funding from KronosBio, Novartis, Oncopeptides, WNTResearch, and Zentalis Pharmaceuticals, plus personal fees from Amgen and Autolus, unrelated to this work. M.W. is a cofounder and shareholder of MSAID GmbH and a scientific advisor of Momentum Biotechnologies, but he has no operational role in either company. The remaining authors declare no competing interests.

Additional information

Supplementary information The online version contains supplementary material available at https://doi.org/10.1038/s41467-026-70394-3.

Correspondence and requests for materials should be addressed to Mohieddin Jafari.

Peer review information *Nature Communications* thanks Francesca Sacco and the other anonymous reviewer(s) for their contribution to the peer review of this work. A peer review file is available.

[1]Department of Biochemistry and Developmental Biology, Faculty of Medicine, University of Helsinki, Helsinki, Finland. [2]Biozentrum, University of Basel, Basel, Switzerland. [3]Institute for Molecular Medicine Finland (FIMM), Helsinki Institute of Life Science, University of Helsinki, Helsinki, Finland. [4]Technical University of Munich, Munich, Germany. [5]Munich Data Science Institute (MDSI), Garching, Germany. [6]Department of Pharmacology, Faculty of Medicine, University of Helsinki, Helsinki, Finland. [7]School of Natural Sciences, Macquarie University, North Ryde, New South Wales 2109, Australia. [8]iCAN Digital Cancer Medicine Flagship, University of Helsinki, Helsinki, Finland. [9]Department of Microbiology, Tumor and Cell Biology, Karolinska Institutet, Stockholm, Sweden. [10]Faculty of Medicine and Health Technology, Tampere University, Tampere, Finland. [11]TAYS Cancer Center, Tampere, Finland. [12]Tampere Institute for Advanced Study, Tampere University, Tampere, Finland. [13]These authors contributed equally: Elham Gholizadeh, Ehsan Zangene. [14]These authors jointly supervised this work: Amir A. Saei, Mohieddin Jafari. ✉e-mail: mohieddin.jafari@helsinki.fi